

Journal of Stress Analysis

Vol. 8, No. 2, 2023-24, 19-40



ORIGINAL RESEARCH PAPER

Investigating the Effect of Laser Parameters on Nano-Machining of Silicon Carbide by Response Surface Method Using Molecular Dynamics Simulation

Mojtaba Zolfaghari^{a,*}, Hamed Heydari^b, Alirezai Vanaki Farahan^a, Vahid Tahmas-



- ^a Department of Mechanical Engineering, Arak University, Arak, Iran.
- ^b School of Mechanic Engineering, Shahrekord University, Shahrekord, Iran.
- ^c Department of Mechanical Engineering, Arak University of Technology, Arak, Iran.

Article info

Article history: Received 25 August 2023 Received in revised form 06 February 2024

Accepted 28 February 2024

Keywords:
Nano-machining
Laser
Molecular dynamics
Silicon crbide
Response surface method

Abstract

The ultra-precise machining process of parts is a very advanced method to achieve dimensional accuracy and surface smoothness in the nanometer range for the production of defense, aerospace, optics, and electronics parts. In this research, the nano-machining process of silicon carbide single crystal under the effect of laser is investigated using the molecular dynamics method. Investigating the effects of the parameters of diameter, pulse intensity, and laser advance speed on this process by the response surface method shows that by reducing the advance speed from 150 to 50 meters per second, the diameter increases from 40 to 80 angstroms and the laser pulse intensity increases from 4×10^8 to 10^9W/cm^2 , the values of shear forces, thrust forces, and Von Mises stress of the workpiece are reduced by 36.1%, 23.2%, and 39.3%, respectively. In addition, when the diameter was 40 angstroms, the pulse intensity was 10⁹W/cm², and the laser advance speed was 50m/s, the hydrostatic stress and machining forces were minimized and the machining process was optimized. By comparing the conventional nano-machining and the optimal mode of the laser nano-machining process, the value of shear forces decreased from 1770 nano-Newtons to 1115 nano-Newtons and the value of thrust forces decreased from 1350 nano-Newtons to 1137 nano-Newtons. Finally, the structural changes investigated by the radial distribution function indicate that the laser-assisted nano-machining process produces fewer structural changes along the bonds.

Nomenclature

r_h	Radius of the laser	V_{sub}	Volume of the desired substructure
P	Laser pulse intensity	P_0	Laser power
r_{laser}	RRadial position	D	Diameter
V	Advanced speed of the laser	N	Number of available atoms

^{*}Corresponding author: M. Zolfaghari (Assistant Professor)

E-mail address: m_zolfaghari@araku.ac.ir doi 10.22084/JRSTAN.2024.28243.1248

ISSN: 2588-2597



1. Introduction

The machining process has advanced significantly, allowing for the precise production of small parts and expanding its applications to different scales. It has led to a smaller one. Additionally, the use of machining to produce complex 3D devices at the nanoscale is clearly an obvious advantage compared to other manufacturing methods [1]. In the field of machining, several fundamental analytical models are used to describe and analyze various aspects of the machining process. These models are based on fundamental principles of mechanics, materials science, and thermodynamics, including mechanics of cutting, tool wear models, surface roughness models, heat transfer models, and material removal rate models [2]. In addition, on this scale, inherent measurement problems limit the use of analytical and experimental models. [3]. With the tendency to develop ultra-precise processes that can reach high-quality surfaces at the nanometer level, there is a need for simulation on the nanoscale, and many of the models mentioned are not sufficient for simulation on the nanoscale.

Today, ultra-precise machining of materials such as ceramics in nano dimensions is suffering from problems due to their high hardness and strength. To mention a few adverse effects of machining ceramic materials, we can highlight the high stresses and forces involved in the process, which can potentially damage the equipment. One such hard ceramic material is silicon carbide (SiC), which has a diamond network structure consisting of relatively high-hardness silicon and carbon, along with semiconducting properties and very high thermal resistance. The properties of this material have made it useful in important industries such as optics, microelectronics, and solar panels. There is also a need to produce parts with a tolerance range in nanometer dimensions from SiC in these industries. However, the hardness of this material and the resulting machining forces are significant on this scale. One method of reducing the hardness and strength of the material during the machining process is laser machining [3, 4]. In this method, by applying a laser, the process of thermal softening occurs in that place, and as a result, machining occurs easily and in more favorable conditions. Practically, conducting repeated experimental tests to investigate the effects of laser components on machining requires spending a lot of money and time, so the need to conduct research and numerical simulations in this field is felt.

The multiscale method (MD+FEM) combines molecular dynamics and finite element method to model material deformation on different length scales, providing insights into cutting force, stress distribution, temperature, and microstructure evolution during nano-cutting, making it a promising tool for optimizing machining parameters and improving surface

quality and functional performance of machined parts [4].

In 2011, Goel et al. investigated the soft behavior of SiC single crystal in the nano-machining process. They chose the Tersoff potential function for the interaction among all atoms and modeled the tool of this process as non-rigid with a negative rake angle. In this process, they calculated the machining temperature and radial distribution function, and in addition, they studied the coating and penetration of atoms in the tool [5]. In 2012, Luo et al. studied and investigated the machinability of SiC single crystal structures by the molecular dynamics method and compared the simulation results with silicon. Their investigations included cut and thrust forces, workpiece temperature, and radial distribution function. By considering the blade as non-rigid, they checked the amount of penetration of atoms in the tool. Also, the rake angle (Rake angle is the angle between the cutting tool bit and the cutting chips of the modeled tool was considered negative for simulation [6]. In 2015, Chavoshi et al. studied the plastic deformation of SiC during the nano-machining process. They investigated this process under different temperatures and by two functions of the Tersoff potential and analytic bond-order potential (ABOP) (Analytic bond-order potential, The ABOP potential is a reformulation of the Tersoff potential as implemented in atomicrex and Lamps.). In addition to studying plastic deformation and dislocations, they investigated machining force, Von Mises stress, and the relationship between this stress and temperature. They modeled the beam as non-rigid with a negative rake angle [7].

In 2015, Xiao et al. investigated the effect of chipping depth on structural changes and cracking in the nano-machining process of a SiC single crystal workpiece. By examining factors such as hydrostatic stress and the position of atoms, they investigated the creation of cracks and structural changes and compared their results with experimental data [8]. In 2016, Dai et al. studied and investigated the chipping of singlecrystal silicon under the laser grinding process. They investigated the damages under the structure and the effects of laser on this process, and the effects of components such as advance speed, diameter, and intensity of laser pulse on the movement path of atoms, phase change of the structure, temperature distribution, machining forces, and friction coefficient were investigated. By comparing the process of nano-machining using laser and traditional nano-machining, they concluded that laser can have a good performance in the process of nano-machining. The blade in this research is modeled as solid and spherical, and the laser is modeled as Gaussian heat flux [9]. In 2017, Wu et al. studied the nano-machining process of SiC single crystal. They modeled the chipping tool rigidly and studied the effect of depth of cut on the plastic deformation of the cutting area, gaps created on the machining path,

chip shape, temperature, and Von Mises stress, and used the radial distribution function to investigate the subsurface damage [10].

In 2017, Bo Zhu et al. studied the vibrationassisted nano-machining process on the SiC single crystal material. The purpose of this research was to investigate the effect of this process on the surface quality and softening of silicon. They chose the Tersoff and Morse interatomic potential and investigated the effect of this process on the components of temperature, tangential force, thrust force, structural changes, and chip formation [11]. In 2017, Dai et al. studied the nano-machining process of single-crystal silicon using a groove tool. They investigated the effect of the angle, depth, width, and shape of the groove tool on the components of temperature, hydrostatic stress, Von Mises stress, machining force, friction, and structural changes. In this research, the Tersoff potential was considered for interaction between silicon atoms and the Morse potential for interaction between silicon and carbon atoms [12]. In 2019, Abdulkadir et al. investigated the effect of tool-tip radius on the nanomachining process of silicon. They investigated the effect of this component on results such as hydrostatic stress, Von Mises stress, machining forces, and friction kinetic energy [13]. In 2018, Liu et al. investigated the nano-machining process of polycrystalline SiC. In this research, they investigated the effect of machining speed and depth on machining components such as temperature, tension, and machining force. In addition, they studied structural changes, subsurface damage, and fracture processes caused by high speeds. In this research, the chipping tool is modeled as spherical and rigid [14]. In 2019, Meng et al. investigated the effect of surface machining on the nano-machining process of SiC single crystal. They studied different manufacturing surfaces of sinusoidal, stepped, and smooth surfaces of this material and investigated the dimensional effects of these surfaces on surface damage, structural deformation, temperature, hydrostatic stress, and tool coating. The tool studied in this research is considered non-rigid to study penetration in the tool [15].

In 2019, Tian et al. investigated the nanoscale machining process on H4 and H6 single-crystal SiC By applying cutting depth and speeds, they investigated the process of structural change and formation of amorphous structure. In addition, they compared the machining forces in both materials [16]. In 2019, Liu et al. studied the stress-assisted nano-machining process on 3C SiC. They studied the effect of auxiliary stress on machining force, distribution of hydrostatic stress, and structural changes of the workpiece. In addition, they used shear strain as a measure of changes from crystalline structure to amorphous structure. In the research, the ABOP potential was used for the interaction among all the atoms in the structure, and the blade was considered rigid [17].

Nano-scale machining can be defined as an ultraprecise manufacturing process by the method of material removal, in which the dimensions of the chip removed from the workpiece and the dimensional accuracy of the final product are close to 100 nm or less. Nano-machining is a method to produce parts with sub-micron dimensional accuracy and final atomic surface smoothness. This process is done due to the separation of a small number of atoms from the surfaces [18]. The process of nanometer machining or nanomachining using a single crystal diamond tool is aimed at achieving nanometer surface smoothness. Using this process, brittle parts such as silicon, and SiC can be easily machined. This is despite the fact that traditional machining of SiC is not possible in practice. In recent years, laser-assisted machining has been proposed as a tool to achieve a higher degree of material separation and improved wear in the machining process of ceramic materials, because in laser-assisted nano-machining, a strong laser beam is used as a heat source to heat the material and softening is used before it is separated by a tool, so the laser beam changes the deformation behavior of the material from hard behavior to soft behavior during machining. Laser-assisted nano-machining with fast and accurate heating in machining ceramic materials with high hardness and brittleness reduces subsurface damage and improves surface integrity compared to traditional nano-machining methods. This process can produce much better workpiece surface quality with higher stock removal rates, lower cutting forces, and moderate tool wear [19].

SiC has unique properties that make it suitable for various nanoscale device applications, such as highpower and high-frequency electronics, sensors, and op-Molecular dynamics simulations can toelectronics. aid in the development and optimization of fabrication processes for these devices, enabling better control over their performance and functionality. In this research, molecular dynamics simulation of the laser nano-machining process was performed for SiC. After extracting the results from the molecular dynamics method, analyzing, investigating, and finding a suitable regression equation to investigate the effects of the components of radius, pulse intensity, and laser advance speed on the force, temperature, Von Mises stress, and hydrostatic stress parameters of the nanomachining process was done using the response surface method (RSM), and then the multi-objective optimization of the nano-machining process was carried out to minimize the machining forces and hydrostatic stress using the hill climbing method.

Overall, this research contributes to understanding of the laser-assisted nano-machining process for SiC single crystal, providing insights into the optimization of parameters and the resulting improvements in dimensional accuracy, surface smoothness, and structural changes. These findings have potential applica-

tions in the production of defense, aerospace, optics, and electronics parts, where ultra-precise machining is required in the nanometer range.

2. Molecular Dynamics Simulation

An overview of the parameters, the geometry of the tool, and the workpiece in the machining process are shown in Fig. 1.

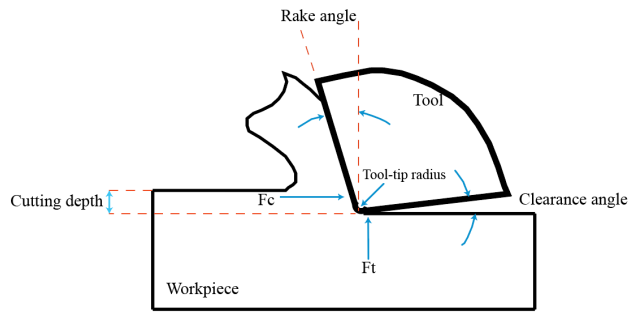


Fig. 1. A view of the machining components [20].

Geometric modeling in this research includes two parts in LAMMPS [21] software. The first part of the beta-phase SiC workpiece with a cubic diamond structure of zinc blende and a lattice constant of 4.3596 angstroms, and the second part is a diamond cutting tool in a cubic diamond structure with a lattice constant of 3.567 angstroms. The blade tool is modeled in such a way that the clearance and rake angles and the tool-tip radius are taken into account, Fig. 1. The workpiece and the cutting tool are modeled as single crystal material and other geometric information of the models created in this research are given in Tables 1 and 2.

Table 1 Geometric characteristics of the workpiece [20, 22].

Parameter (unit)	Value
Length (A ⁰)	259
Width (A^0)	84
Height (A^0)	92
Height (A^0)	92

Table 2 Geometric characteristics and tool position [20, 22].

Parameter (unit)	Value
Tool-tip radius(A^0)	10
Clearance angles	9.5
Rake angles	10.5
Cutting depth (A^0)	15
Width tool (A^0)	84
The distance between the tip of the tool	10
and the workpiece (A^0)	10

The direction of cutting or movement of the model tool created in LAMMPS is in the direction of [0 1 0]

and the cutting plane of the workpiece is the plane (0 0 1), Fig. 2.

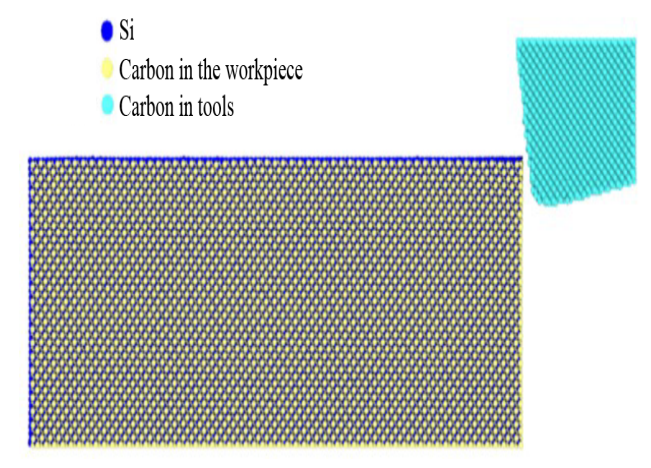


Fig. 2. View of the created model of the workpiece and the cutting tool in the OVITO software.

In this research, the Tersoff potential function is used for the interaction of silicon atoms inside the workpiece, between carbon atoms inside the workpiece, between carbon and silicon atoms inside the workpiece, between silicon atoms of the workpiece and carbon of the tool, and between carbon atoms of the workpiece and carbon of the tool [23]. The interaction between the carbon atoms inside the structure of the tool is ignored and considered rigid. In this way, the coefficients of the Tersoff potential function in Table 3 are used in the simulation.

Table 3
Tersoff potential function coefficients used in the present study [23].

Potential function	C	C-Si	Si
coefficients (unit)	C	0-51	O1
$D_0(ev)$	6.00	4.36	3.24
$r_0(A)$	1.4276	1.79	2.222
S	2.167	1.847	1.57
$\beta(A^{-1)}$	2.0099	1.6991	4760/1
γ	0.11233	0.011877	0.09253
p	181.910	273987	1.13681
q	6.28433	180.314	0.63397
h	0.5556	0.68	0.335
$\lambda_3(A^{-1})$	0	0	0
R(A)	2.00	2.40	2.90
D(A)	0.15	0.20	0.15

The atoms that make up the workpiece are classified into three groups: boundary atoms, thermostat atoms, and Newtonian atoms. Fig. 3 shows how to apply these boundary conditions to the workpiece.

The ensemble used is the Microcanonical ensemble NVE with a time step of one femtosecond in 100,000-time steps. The laser application process is in the form

of thermal flux, Fig. 4, and the surface laser pulse intensity is modeled as a Gaussian distribution, which is expressed according to Eq. (1) [19].

$$P(r_{laser}) = \frac{2P_0}{\pi r_h^2} \exp\left(-\frac{2r_{laser}^2}{r_h^2}\right) \tag{1}$$

Where r_h is the radius of the laser, P is the laser pulse intensity, P_0 is the laser power, and r_{laser} is the radial position.

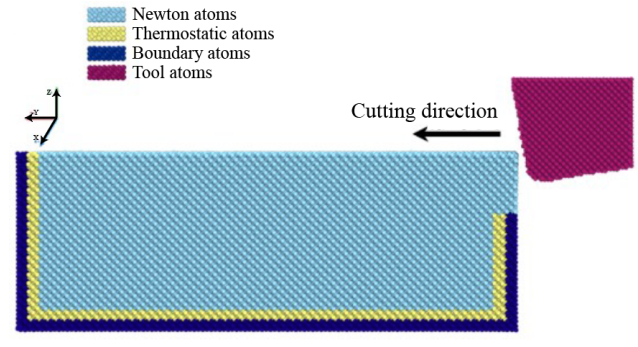


Fig. 3. A view of the simulation model with boundary conditions.

3. Experiment Design

In order to perform the RSM, it is necessary to design an experiment to fit the data. The input factors are diameter, pulse intensity, and laser advance speed, Table 4, and machining force, hydrostatic stress, and von Mises stress are the answers.

The design of the experiment was carried out by the central composite method and the number of input variable factors in the experiment is three, Table 5

Table 4
Range of input factors in RSM [9, 19].

Factor	Range of values
Diameter of the laser (A^0)	40-80
laser pulse intensity (W/cm^2)	4×10^8 - 10^9
advance speed (m/s)	50-150

4. Validation

The accuracy of the simulation process is checked by comparing the results of this research with the results of the research conducted by Dai et al. [19] on single-crystal silicon material. By looking at Fig. 5, it can be seen that the maximum location of the atoms of the workpiece in the simulation is 139 angstroms and the minimum is 66 angstroms, so it can be seen that the changes in the position of the atoms of the workpiece in the simulation are in a good agreement with the results of the article. Fig. 6 shows a comparison of the temperature contour of the workpiece in the simulation and the results of the reference research [19], by looking at this figure, it can be seen that there is a suitable match between the temperature results in these two processes.

Another one of these discussed results is the machining force. According to the diagram in Fig. 7, it can be seen that the machining forces are also in good agreement with the results of reference [9] based on the created model.

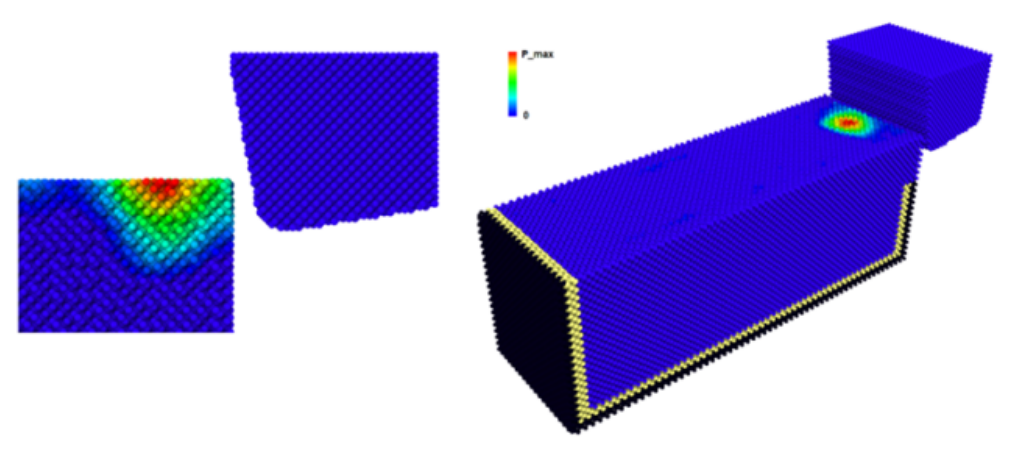


Fig. 4. The view of the final simulation model with a cut view

Table 5
Table of experimental design in response surface method.

No.	1	2	3	4	5	6	7	8	9	10	11	12	13	14	15
Diameter of the laser (A ⁰)	80	60	60	40	60	60	80	40	40	80	80	60	40	40	80
Laser pulse intensity (W/cm^2)	10^{9}	7×10^8	10^{9}	4×10^8	7×10^8	4×10^8	10^{9}	10^{9}	7×10^8	4×10^8	4×10^8	7×10^8	4×10^8	10^{9}	$7{\times}10^{8}$
Advance speed (m/s)	150	150	100	150	50	100	50	150	100	150	50	100	50	50	100

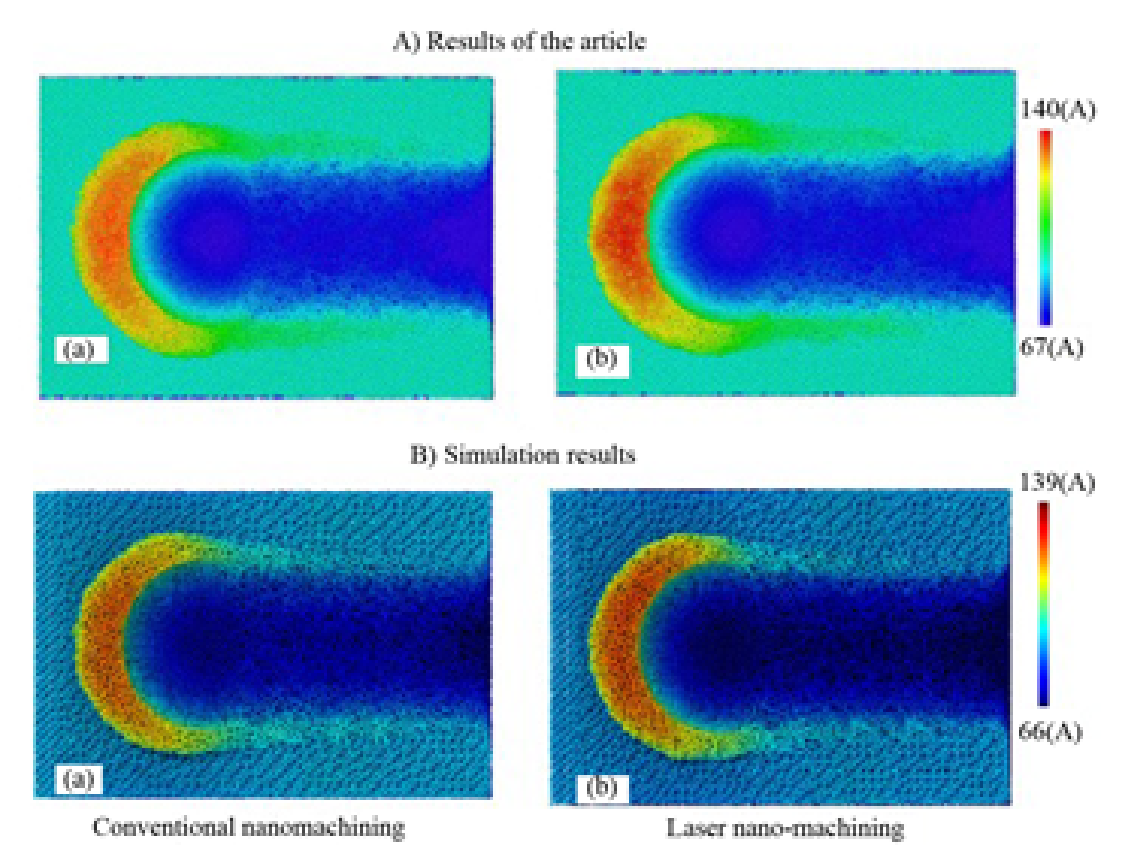


Fig. 5. Location of the atom in a) Reference [19] b) Simulation of the present study.

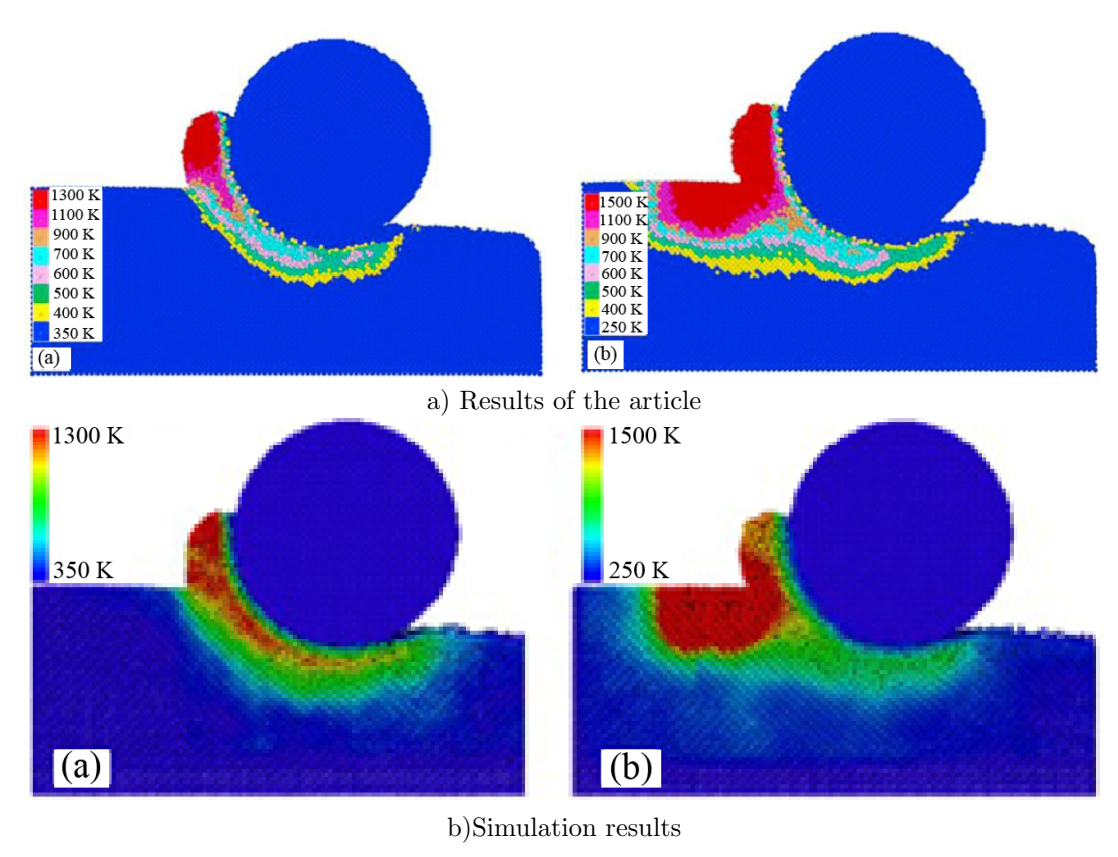


Fig. 6. Temperature contour a) Reference [19] b) Simulation of the present research at the position of 155 Angstroms.

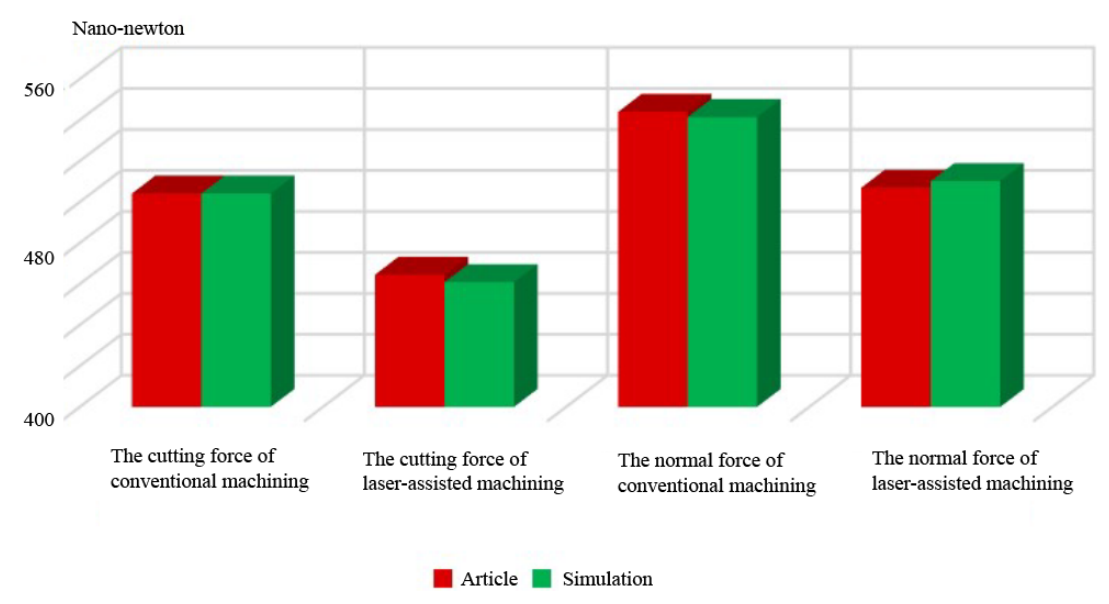


Fig. 7. Bar graph of force results.

Table 6
Simulation results.

No	Diameter of	laser pulse intensity	advance	Cutting	Thrust	Hydrostatic	Von Mises	Surface temperature
INO	the laser (A^0)	(W/cm^2)	speed (m/s)	force (nN)	force (nN)	stress (GPa)	stress (GPa)	(^{0}K)
1	80	10^{9}	150	1652.87	1397.54	4.41	12.09	915
2	60	$7*10^8$	150	1714. 69	1439.56	3.80	11.07	836
3	60	10^{9}	100	1602.85	1371.06	3.81	11.09	902
4	40	$4*10^8$	150	1741. 56	1480.38	3.56	10.86	810
5	60	$7*10^8$	50	1387. 24	1178.36	3.20	8.94	952
6	60	$4*10^8$	100	1745. 67	1480.29	3.78	11.02	833
7	80	10^{9}	50	1115.52	1137.84	3.05	7.34	1022
8	40	10^{9}	150	1771.55	1443.62	3.65	10.89	832
9	40	$7*10^8$	100	1717. 31	1435.80	3.67	10.98	834
10	80	$4*10^8$	150	1728.67	1444.07	3.89	11.17	832
11	80	$4*10^8$	50	1510.92	1266.68	3.06	8.10	916
12	60	$7*10^8$	100	1614.8	1409.82	3.71	11.01	848
13	40	$4*10^8$	50	1629.63	1413.21	3.32	10.24	862
14	40	10^{9}	50	1531.97	1290.74	3.12	8.76	920
15	80	$7*10^8$	100	1531.97	1406.01	3.84	11.16	875

Based on all the results observed in this section, it can be seen that the simulation process is correct and the results can be cited.

5. Response Surface Method

The response surface method (RSM), which is implemented by Design Expert software, is performed to approximate the behavior of laser-assisted nanomachining based on the input components of pulse intensity, advance speed, and laser diameter. The simulation outputs of the nano-machining process are the cutting force, thrust force, hydrostatic stress, von Mises stress in the workpiece, and the average temperature of the cutting area, Table 6.

According to the obtained results, Table 6, appro-

priate regression equations and their coefficients are calculated to determine the behavior of the outputs of this process and its changes in the fourth section. The least squares method is used to estimate the approximate coefficients of polynomial models [24].

5.1. Response Surface for Cutting Force

The cutting force resulting from the nano-machining process is the sum of the interaction forces between the atoms of the workpiece and the tool in the direction of the movement of the tool, which is the result of the interatomic energy level gradient. The cutting force regression equation is Eq. (2):

$$F_c^2 = \beta_0 + \beta_1 D + \beta_2 P + \beta_V + \beta_{12} DP + \beta_{13} DV + \beta_{23} PV + \beta_{11} D^2 + \beta_{22} P^2 + \beta_{33} V^2$$
 (2)

D is the diameter, P is the pulse intensity, and V is the advanced speed of the laser. After introducing the cutting force regression model, the variance analysis of the input factors is performed according to Table 7.

The selected second-order equation and the value of R^2 , R^2_{adj} , and R^2_{pre} of this model are 98.8, 96.7, and 82.8% respectively. Since the difference between

 R_{adj}^2 and R_{pre}^2 is less than 20%, the presented model is suitable. According to Table 7, it can be seen that the D^2 factor, whose F value is greater than 0.05, is less effective and this component can be ignored. After obtaining the coefficients of the equation and variance analysis, Eq. (3): will be the cutting force response surface equation.

$$F_c^2 = 3.27 \times 10^6 - 5571.2D - 0.003P + 1.24 \times 10^4 V - 2.3 \times 10^{-5}DP + 128.03DV + 9.97 \times 10^{-6}PV - 32.99D^2 + 1.63 \times 10^{-12}P^2 - 91.58V^2$$
 (3)

According to the graphs resulting from the analysis of the cutting force response surface, Figs. 8, 9, and 10, it can be concluded that the cutting force decreases with the increase in the diameter and laser pulse intensity, and on the other hand, this happens with the decrease in the advance speed. Reducing the cutting force is desirable and reduces damage to the tool. The

effect of the laser speed and diameter components is greater than the effect of laser pulse intensity on the reduction of cutting force. This shows that increasing the area of application of heat to the atoms in the workpiece and increasing the time for heat transfer will significantly reduce the hardness and strength of the workpiece [9,19].

Table 7
Variance analysis of cutting force response surface.

Parameter	Sum of squares	Average of squares	F value	P value
D	6.39×10^{11}	6.39×10^{11}	76.25	0.0003
P	3.91×10^{11}	3.91×10^{11}	46.58	0.001
V	1.92×10^{12}	1.92×10^{12}	228.51	< 0.0001
DP	1.49×10^{11}	1.49×10^{11}	17.76	0.0084
DV	1.31×10^{11}	1.31×10^{11}	15.64	0.0108
PV	1.79×10^{11}	1.79×10^{11}	21.33	0.0057
D^2	4.47×10^{8}	4.47×10^{8}	0.053	0.8264
P^2	5.56×10^{10}	5.56×10^{10}	6.63	0.0498
V^2	$1.35{ imes}10^{11}$	$1.35{ imes}10^{11}$	16.07	0.0102

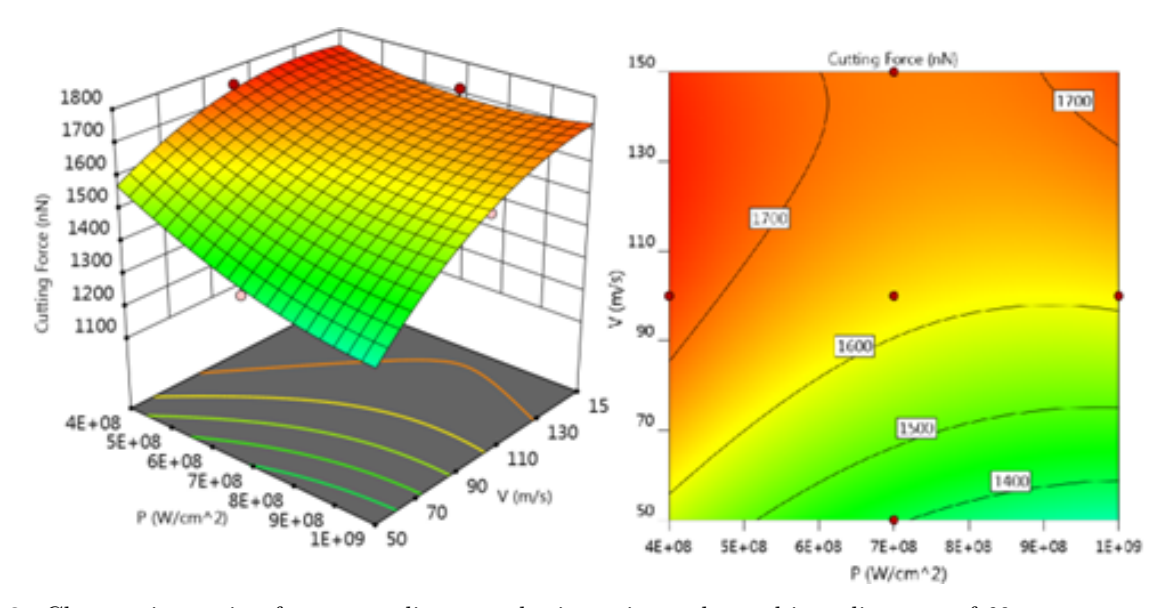


Fig. 8. Changes in cutting force according to pulse intensity and speed in a diameter of 60 angstroms.

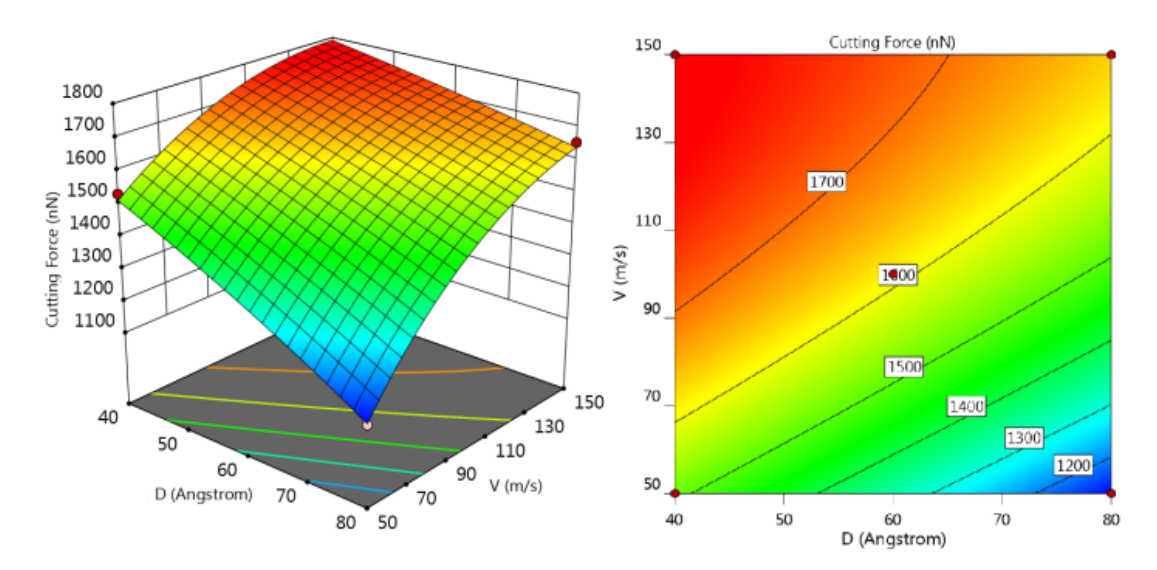


Fig. 9. Changes of cutting force per diameter and speed at pulse intensity of $7 \times 10^8 \text{W/cm}^2$.

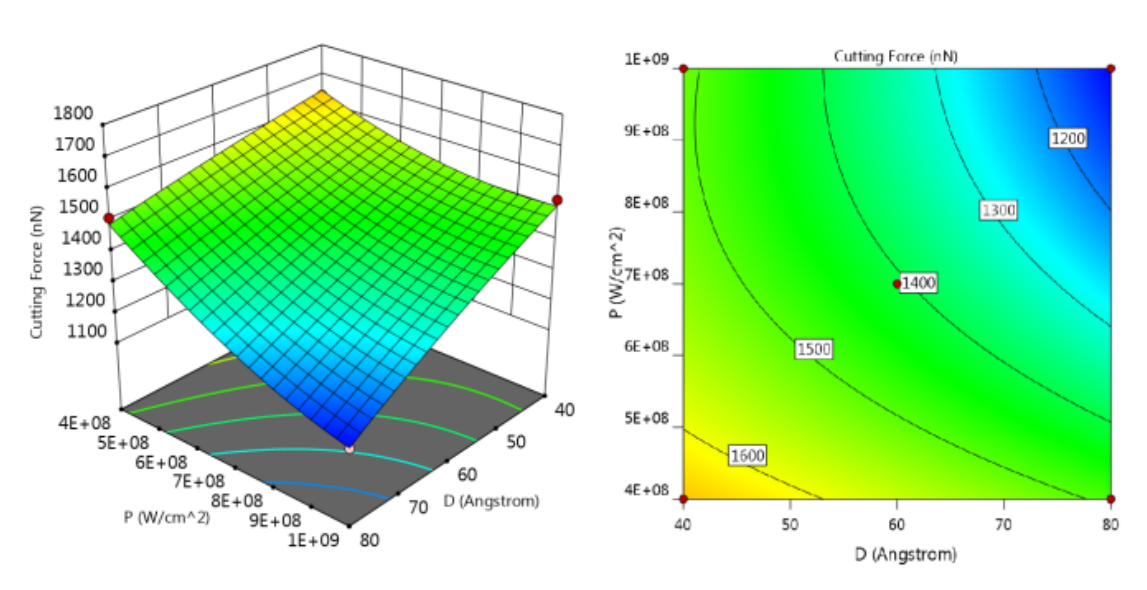


Fig. 10. Changes in cutting force for pulse intensity and diameter at a speed of 50m/s.

5.2. Response Surface for Thrust Force

The thrust force resulting from the nano-machining process is the sum of the interaction forces between the atoms of the workpiece and the tool perpendicular to the machining surface. Eq. (4): is the regression equation of the thrust force caused by machining.

$$\sqrt[3]{F_T} = \beta_0 + \beta_1 D + \beta_2 P + \beta_3 V + \beta_{12} DP + \beta_{13} DV
+ \beta_{23} PV + \beta_{11} D^2 + \beta_{22} P^2 + \beta_{33} V^2$$
(4)

After introducing the thrust force regression model, the variance analysis of the input factors has been performed according to Table 8.

The selected second-order equation and the value of R^2 , R_{adj}^2 , and R_{pre}^2 of this model are 96.2, 89.3, and 68.9% respectively. Since the difference between R_{adj}^2

and R_{pre}^2 is almost less than 20%, the presented model is suitable. According to Table 8, the effective factors in Eq. (4): are P, D, V, and V^2 . Therefore, after obtaining the coefficients of the equation, Eq. (4):, the equation of the response surface of the thrust force will be in the form of Eq. (5):

$$\sqrt[3]{F_T} = 11.91 - 0.031D - 1.86 \times 10^{-9}P + 0.0177V
- 1.53 \times 10^{-12}DP + 7.9 \times 10^{-5}DV
+ 4.12 \times 10^{-12}PV + 1.52 \times 10^{-4}D^2
+ 8.10 \times 10^{-19}P^2 - 10^{-4}V^2$$
(5)

The figures resulting from the analysis of the response surface of the thrust force machining in terms of diameter, pulse intensity, and laser advance speed are shown in Figs. 11, 12, and 13.

 ${\bf Table~8} \\ {\bf Variance~analysis~of~thrust~force~response~surface}.$

Parameter	Sum of squares	Average of squares	F value	P value
D	0.1301	0.1301	13.99	0.0134
P	0.1483	0.1483	15.95	0.0104
V	0.6416	0.6416	69.01	0.0004
DP	0.0007	0.0007	0.0724	0.7986
DV	0.05	0.05	5.38	0.0681
PV	0.0306	0.0306	3.29	0.1295
D^2	0.0095	0.0095	1.02	0.3581
P^2	0.0137	0.0137	1.47	0.2793
V^2	0.1652	0.1652	17.77	0.0084

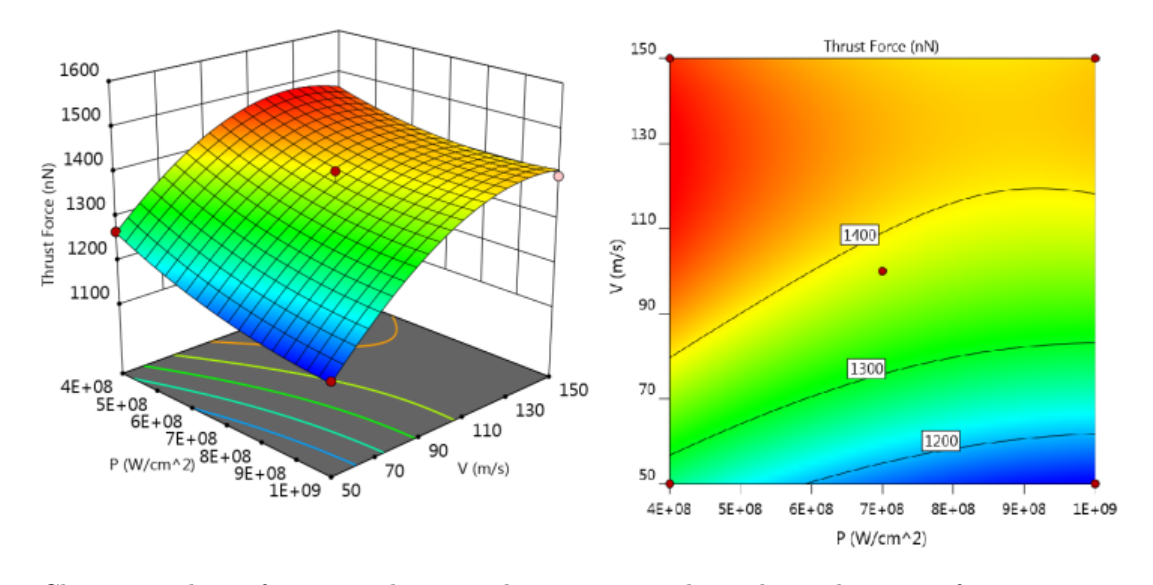


Fig. 11. Changes in thrust force according to pulse intensity and speed in a diameter of 80 angstroms.

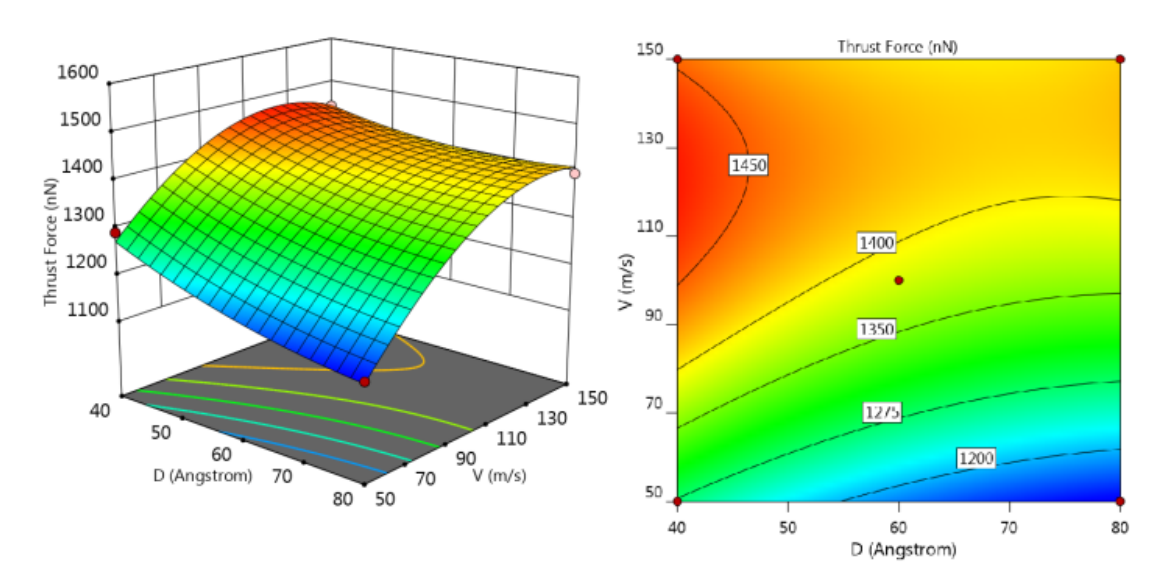


Fig. 12. Changes of thrust force per diameter and speed at pulse intensity of $10^9 \mathrm{W/cm^2}$.

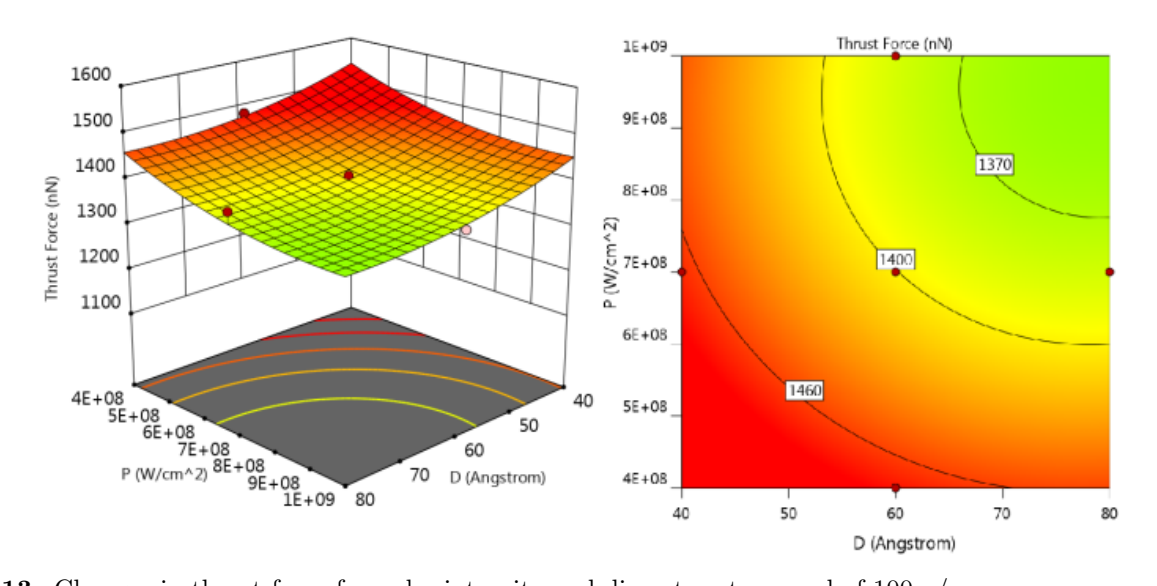


Fig. 13. Changes in thrust force for pulse intensity and diameter at a speed of 100m/s.

According to Figs. 11, 12, and 13, we can conclude that with increasing diameter, increasing laser radius, and decreasing laser advance speed, the thrust force as well as the cutting force decrease. Reducing the speed compared to the increase of other components has a greater effect on the reduction of the thrust force because the time of heat transfer on the surface of the workpiece increases with the reduction of the laser advance speed. As a result, the kinetic energy of more layers of the underlying atoms increases. This process increases the level of kinetic energy among the atoms and changes the interatomic distance, and on the other hand, the interatomic bond becomes unstable; therefore, less energy and force are consumed to destroy the interatomic bond and compress the atomic layers of the workpiece surface.

5.3. Response Surface for Hydrostatic Stress

The hydrostatic stress in molecular dynamics for a structure with a certain volume is obtained by Eq. (6) [25]:

$$\sigma_H = \frac{\sum_{1}^{N} (\sigma_{xx} + \sigma_{yy} + \sigma_{zz})}{3V_{sub}} \tag{6}$$

In Eq. (6), V_{sub} is the volume of the desired substructure and N is the number of available atoms. The regression equation of hydrostatic stress is obtained based on the components of diameter, pulse intensity, and laser advance speed, Eq. (7).

$$\sigma_H = \beta_0 + \beta_1 D + \beta_2 P + \beta_3 V + \beta_{12} DP + \beta_{13} DV + \beta_{23} PV + \beta_{11} D^2 + \beta_{22} P^2 + \beta_{33} V^2$$
(7)

After introducing the hydrostatic stress regression model, the variance analysis of the input factors has been performed according to Table 9.

Table 9
Variance analysis of hydrostatic stress results

Parameter	Sum of	Average of	F	\overline{P}
1 arameter	squares	squares	value	value
D	0.0878	0.0878	20.79	0.0061
P	0.0196	0.0196	4.65	0.0836
V	1.28	1.28	303.93	0.0001
DP	0.0470	0.0470	11.13	0.0207
DV	0.2550	0.2550	60.41	0.0006
PV	0.0820	0.0820	19.43	0.0070
D^2	0.0004	0.0004	0.0857	0.7815
P^2	0.0030	0.0030	0.7157	0.4362
V^2	0.1777	0.1777	42.09	0.0013

The selected second-order equation and the value of R^2 , R_{adj}^2 , and R_{pre}^2 are 98.9%, 97.1%, and 85.9%, respectively. Since the difference between R_{adj}^2 and R_{pre}^2 is almost less than 20%, the presented model is suitable. The components with a low effect are components P, D^2 , and P^2 , whose effects cannot be considered. Finally, the hydrostatic stress response surface model and its equation coefficients are calculated in the form of Eq. (8).

$$\sigma_H = 3.77 - 0.018D - 1.83 \times 10^{-9}P + 0.013V$$

$$-1.28 \times 10^{-11}DP + 1.79 \times 10^{-4}DV$$

$$+6.75 \times 10^{-12}PV - 3 \times 10^{-4}D^2$$

$$+3.81 \times 10^{-9}P^2 + 1.02 \times 10^{-4}V^2$$
(8)

After obtaining the coefficients of the regression equation, the figures related to the effects of all three components are depicted for the hydrostatic stress, Figs. 14, 15, and 16.

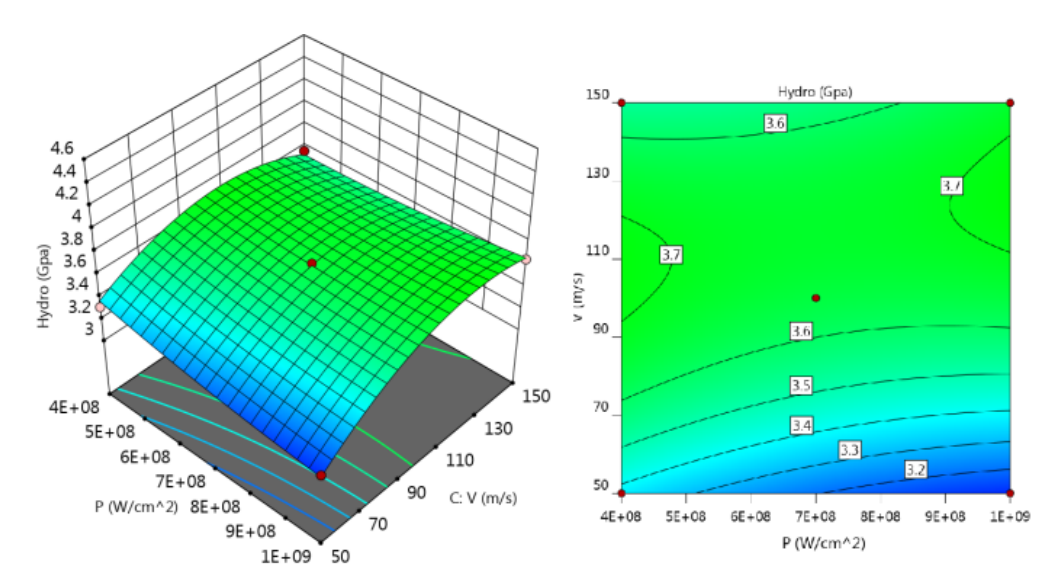


Fig. 14. Changes in hydrostatic stress according to pulse intensity and speed in a diameter of 40 angstroms.

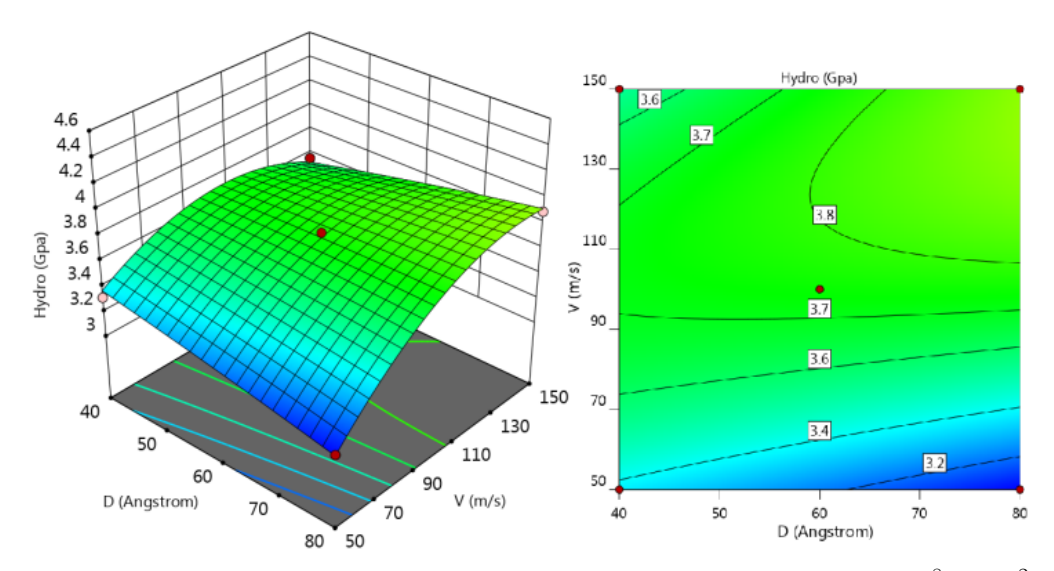


Fig. 15. Changes of hydrostatic stress per diameter and speed at pulse intensity of $4 \times 10^8 \text{W/cm}^2$.

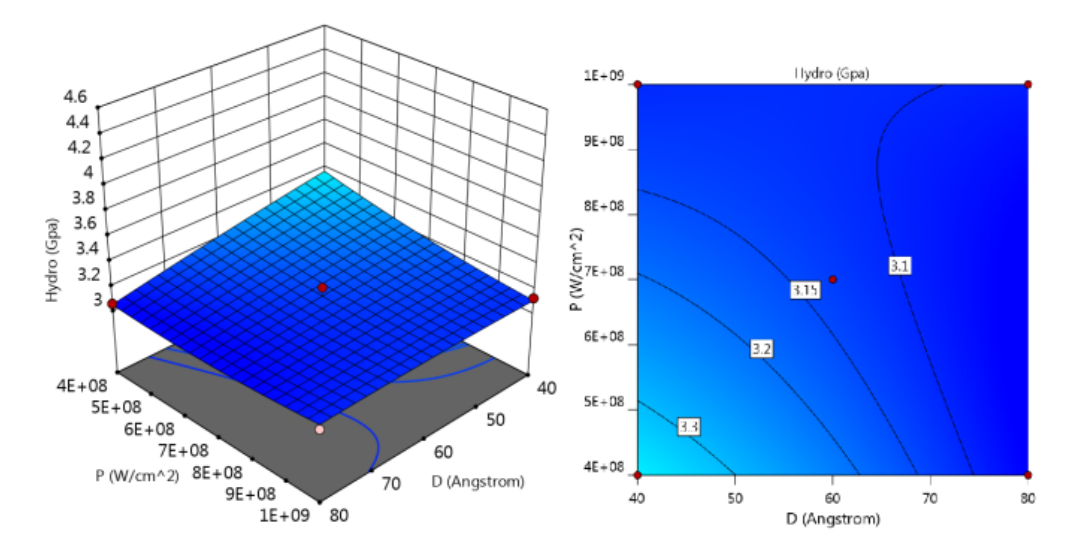


Fig. 16. Changes in hydrostatic stress for pulse intensity and diameter at a speed of 50m/s.

As can be seen in Figs. 14, 15, and 16, with the increase of the laser diameter, the intensity of the laser pulse, and the reduction of its advance speed, the hydrostatic stress decreases, and this reduction in the hydrostatic stress is very small. Since the hydrostatic stress is a measure of how the crystal structure and its volume change in the atomic structure [25-27], and according to Fig. 17, the atomic structure does not show many structural changes between the state in which the minimum and maximum hydrostatic stress is observed, the reason for this is the insignificant changes of hydrostatic stress in different situations. In practice, the amorphous structure formed in the state of the lowest and highest hydrostatic stress is 18.5% and 18.1% of the whole system, respectively, and has not changed much Fig. 18.

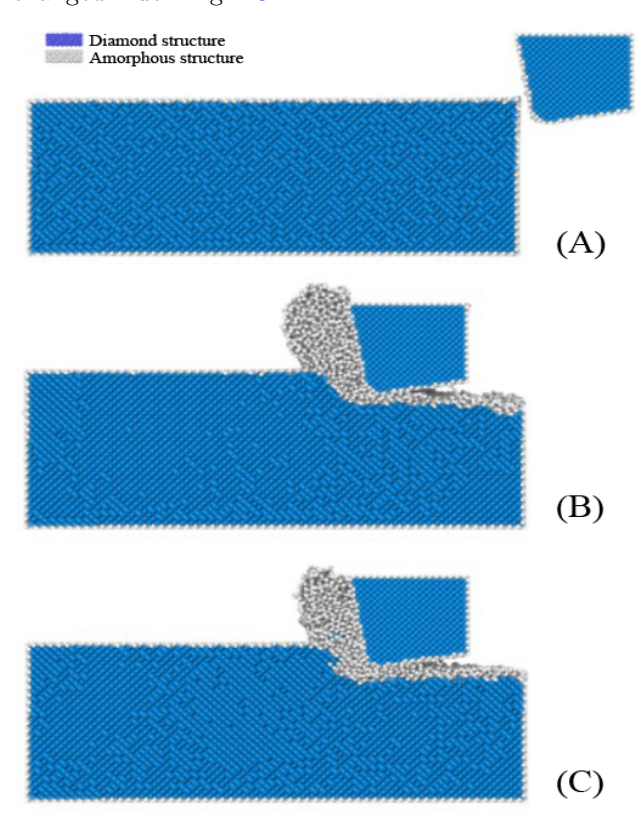


Fig. 17. Figure of the crystal structure A) before machining, B) after machining at the lowest hydrostatic stress, and C) after machining at the highest hydrostatic stress.

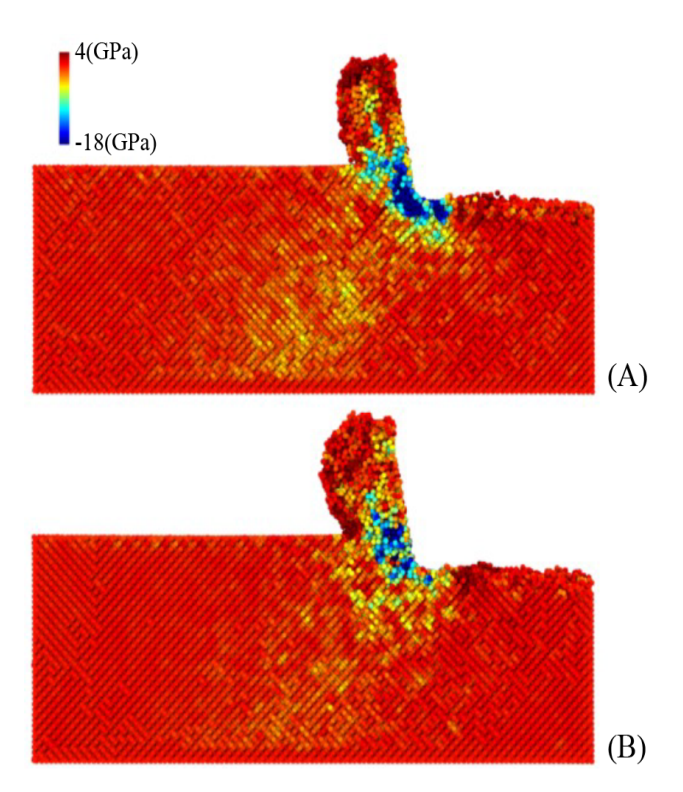


Fig. 18. Hydrostatic stress contour in A) Maximum hydrostatic stress and B) Minimum hydrostatic stress.

In Fig. 18, it can be seen that the local stress in parts A and B are in a good agreement with each other, but in the contact area of the tool in case A, the compressive stress area is slightly higher. In this figure, it can be seen that the hydrostatic stress created in the piece at the contact point of the tool is negative and compressive, and this stress has appeared positively in the whole piece. In general, the compressive stress in front of the tool leads to a change in the volume of the crystal lattices in the contact area of the tool and finally changes the shape of these structures to an amorphous structure.

5.4. Response Surface for Von Mises Stress

The equivalent von Mises stress in molecular dynamics for a structure with a certain volume is obtained by Eq. (9):

$$\sigma_{\nu} = \frac{\sum_{1}^{N} \left(\sqrt{(\sigma_{xx} - \sigma_{yy})^{2} + (\sigma_{yy} - \sigma_{zz})^{2} + (\sigma_{xx} - \sigma_{zz})^{2} + 6(\sigma_{xy}^{2} + \sigma_{yz}^{2} + \sigma_{xz})^{2} \right)}{\sqrt{2} V_{sub}}$$
(9)

 V_{sub} is the volume of a given structure to calculate the stress, N is the number of atoms in the structure, σ_{xx} , σ_{yy} , and σ_{zz} are the vertical components of the stress along the Cartesian coordinates and σ_{xy} , σ_{yz} , and σ_{xz} are the shear component of the stress. The hydrostatic stress regression equation based on the com-

ponents of diameter, pulse intensity, and laser advance speed, Eq. (10), is obtained from the equation of the second-order model of the RSM.

$$\sigma_{\nu} = \beta_0 + \beta_1 D + \beta_2 P + \beta_3 V + \beta_{12} DP + \beta_{13} DV + \beta_{23} PV + \beta_{11} D^2 + \beta_{22} P^2 + \beta_{33} V^2$$
(10)

After introducing the von Mises stress regression model, the variance analysis of input factors is performed according to Table 10.

The selected second-order equation and the value of R^2 , R^2_{adj} , and R^2_{pre} of this model are 98.6%, 96%, and 85.9%, respectively. Since the difference between R^2_{adj} and R^2_{pre} is almost less than 20%, the presented model is suitable. According to Table 9, factors P^2 , V^2 , DV, P, and V are among the factors that have little effect on the outcome of the problem and can be ignored. Finally, the coefficients of the response surface equation are obtained according to Eq. 11.

$$\sigma_{\nu} = 11.75 - 0.09D - 4.53 \times 10^{-9}P + 0.056V + 3.34 \times 10^{-11}DP + 6.34 \times 10^{-4}DV + 2.67 \times 10^{-11}PV - 4.6 \times 10^{-5}D^{2} - 3.96 \times 10^{-19}P^{2} - 4.34 \times 10^{-4}V^{2}$$
(11)

According to the graphs related to the response surface of the average Von Mises stress of the workpiece, Figs. 19, 20, and 21, it can be seen that the value of the Von Mises stress decreases as the diameter in-

creases, the pulse intensity increases and the laser advance speed decreases. By increasing the diameter and intensity of the laser pulse, the effect of thermal softening will increase, and with the increase of this effect, the hardness and strength of the workpiece will decrease.

The von Mises stresses used in the response surface are the average stresses of the atoms in the volume of the workpiece, but the shear zone stresses may have higher values than these numbers. As seen in Fig. 22, the von Mises stress contour indicates that the stress created in the lowest state, state B, occurs when the applied laser beam has its highest performance on the workpiece. This state occurs when the laser used in this process has the largest diameter, the highest intensity of the pulse, and the lowest advance speed. With a lower speed, the laser has the necessary opportunity to heat the atomic layers compared to other test conditions, and the observed surface softening process occurs due to the weakening of the covalent bond between silicon and carbon atoms. Also, the subsurface stresses observed in state B are very low compared to state A, which is a desirable process alone.

Table 10
Variance analysis of von Mises stress response surface.

Parameter	Sum of squares	Average of squares	F value	P value
\overline{D}	0.3435	0.0878	4.63	0.0004
P	0.1480	0.0196	1.99	0.0841
V	16.18	1.28	217.90	0.217
DP	0.3217	0.0470	4.33	< 0.0001
DV	3.21	0.2550	43.27	0.0919
PV	1.29	0.0820	17.35	0.0012
D^2	0.0009	0.0004	0.0118	0.0088
P^2	0.0033	0.0030	0.0440	0.9176
V^2	3.03	0.1777	40.84	0.8422

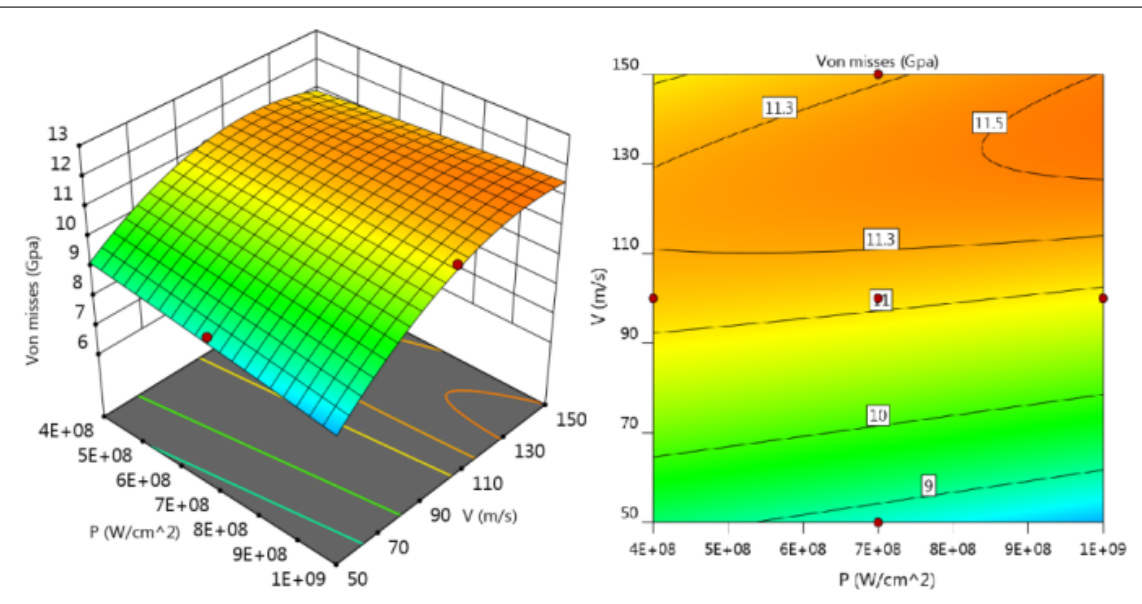


Fig. 19. Changes in hydrostatic stress according to pulse intensity and speed in a diameter of 60 angstroms.

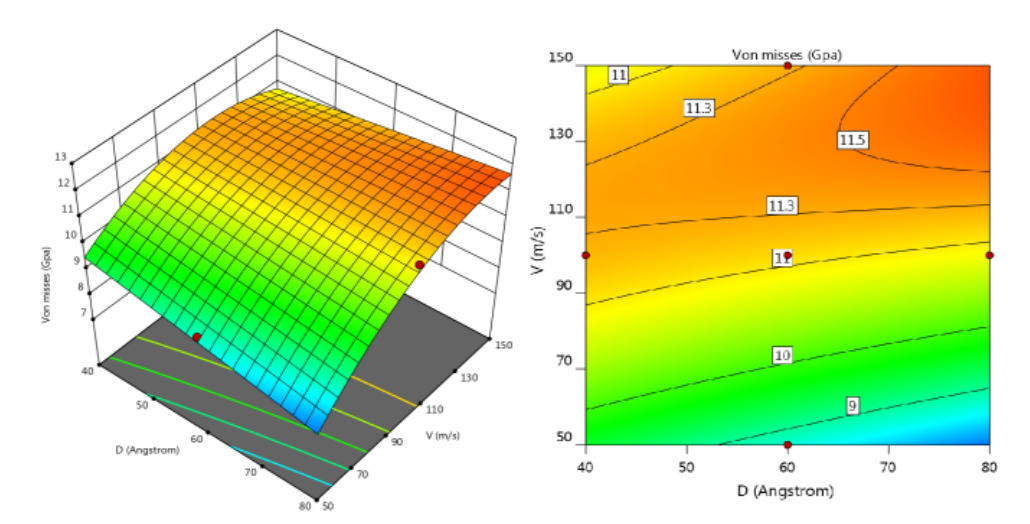


Fig. 20. Changes of hydrostatic stress per diameter and speed at pulse intensity of $7 \times 10^8 \text{W/cm}^2$.

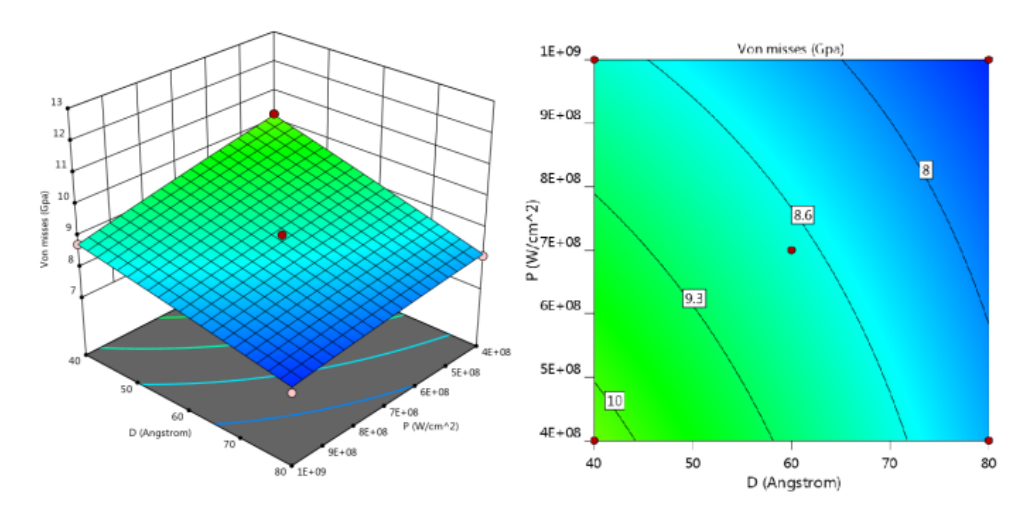


Fig. 21. Changes in hydrostatic stress for pulse intensity and diameter at a speed of 150m/s.

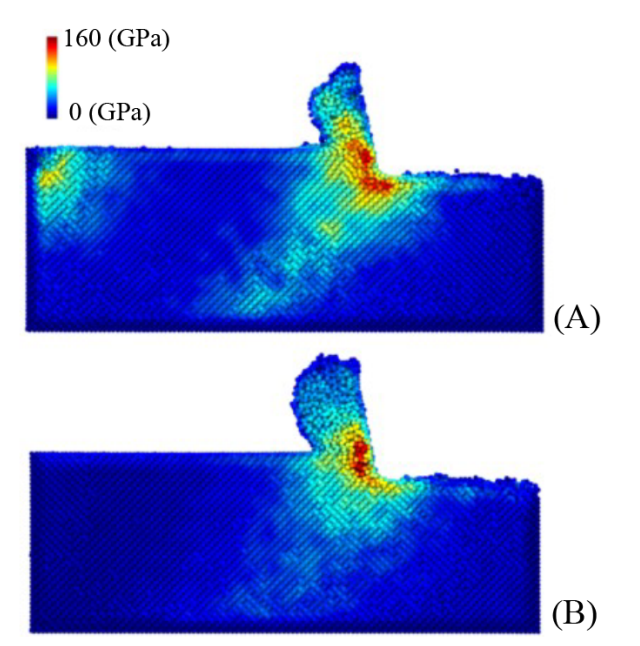


Fig. 22. Von Mises stress contour in a) Minimum state and b) Maximum state.

5.5. Response Surface for Temperature

The regression equation of the average temperature for the workpiece during machining is obtained according to Eq. (12).

$$\sqrt{T} = \beta_0 + \beta_1 D + \beta_2 P + \beta_3 V + \beta_{12} DP + \beta_{13} DV + \beta_{23} PV + \beta_{11} D^2 + \beta_{22} P^2 + \beta_{33} V^2$$
(12)

After introducing the temperature regression model, the variance analysis of input factors is carried out according to Table 11.

The selected second-order equation and the value of R^2 , R^2_{adj} , and R^2_{pre} of this model are 98.12%, 94.7%, and 84.1%, respectively. Since the difference between R^2_{adj} and R^2_{pre} is almost less than 20%, the presented model is suitable. According to Table 10, the effective factors are P, D, V, DP, and V^2 . Finally, the temperature response surface model and its equation

coefficients are in the form of Eq. (13).

$$\sqrt{T} = 29.90 + 0.047D - 9.97 \times 10^{-10}P - 0.046V$$

$$+ 3.65 \times 10^{-11}DP - 9.4 \times 10^{-5}DV$$

$$+ 7.39 \times 10^{-12}PV - 3.16 \times 10^{-4}D^{2}$$

$$+ 1.02 \times 10^{-18}P^{2} + 2.11 \times 10^{-4}V^{2}$$
(13)

From the graphs of the temperature response surface, Figs. (23), (24), and (25), it can be concluded that the workpiece surface temperature increases with increasing diameter, increasing pulse intensity, and decreasing laser advance speed.

Table 11 Variance analysis of temperature response surface.

Parameter	Sum of	Average of	F	\overline{P}
1 arameter	squares	squares	value	value
D	2.53	2.53	51.72	0.0008
P	3.18	3.18	64.84	0.0005
V	5.58	5.58	113.90	0.0001
DP	0.384	0.384	7.84	0.0380
DV	0.071	0.071	1.45	0.2820
PV	0.098	0.098	2.01	0.2160
D^2	0.041	0.041	0.8371	0.4020
P^2	0.021	0.021	0.4401	0.5360
V^2	0.717	0.717	14.65	0.0123

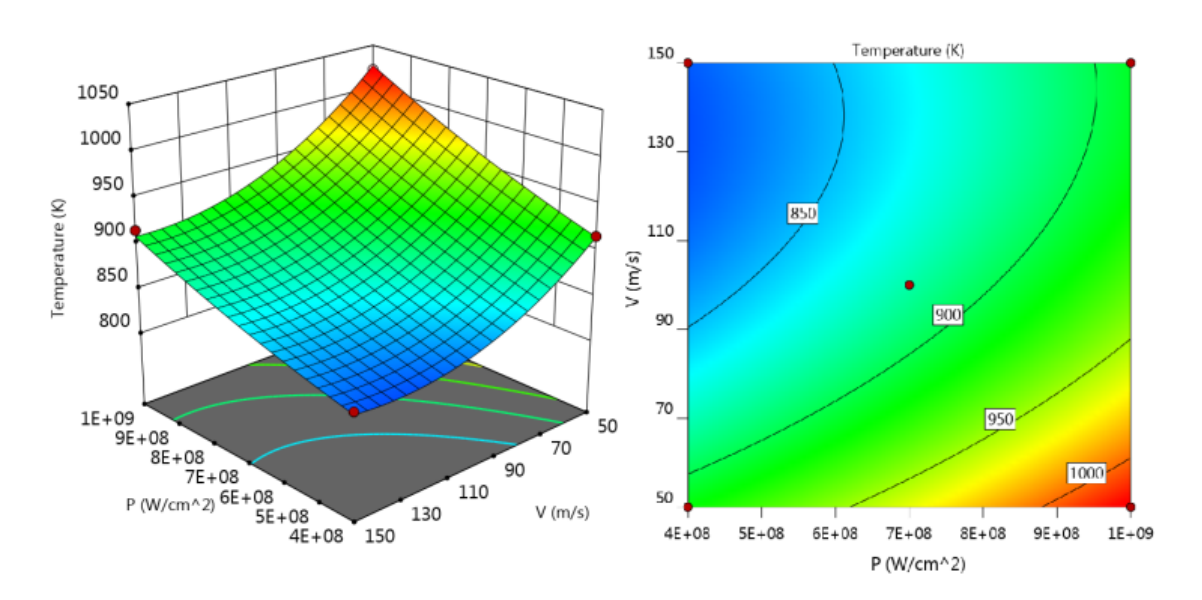


Fig. 23. Changes in temperature according to pulse intensity and speed in a diameter of 80 angstroms.

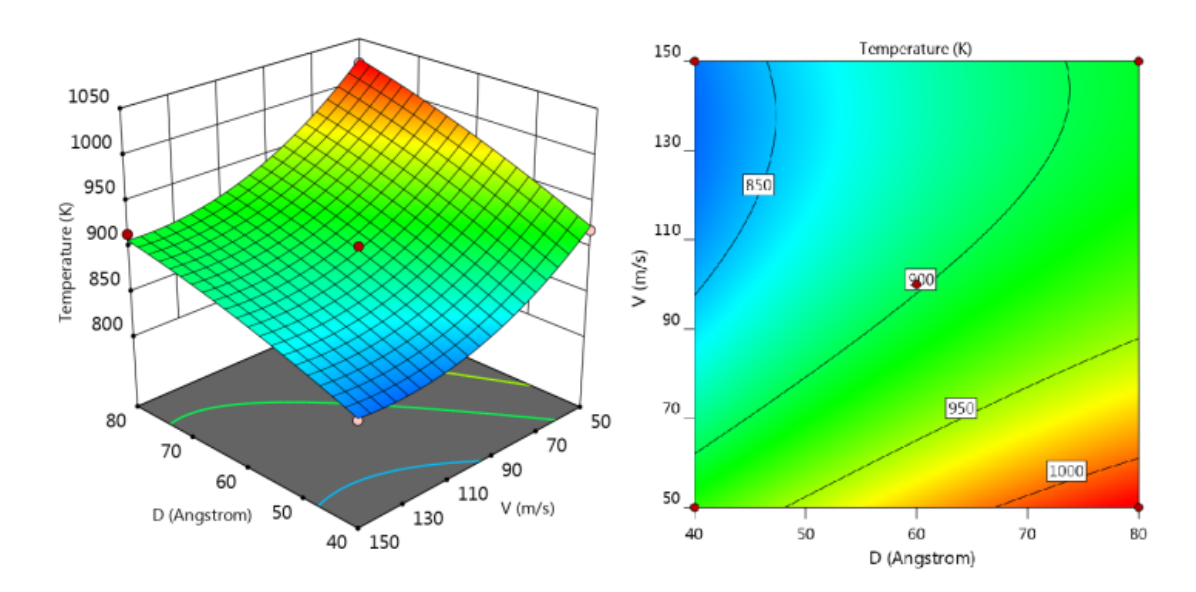


Fig. 24. Changes of temperature per diameter and speed at pulse intensity of 10⁹W/cm².

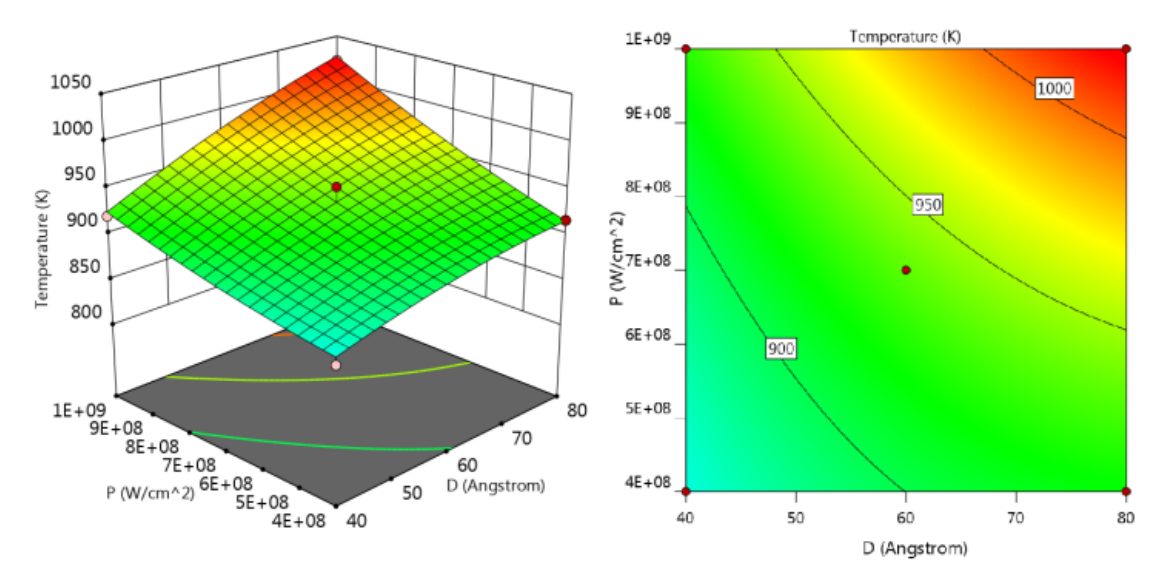


Fig. 25. Changes in temperature for pulse intensity and diameter at a speed of 50m/s.

The temperature created in this process is the result of two processes. The first process is caused by chipping and the second process is caused by applying heat. During the chipping process, a plastic deformation mechanism occurs, which is caused by breaking atomic bonds and finally changing the crystal structure. This breaking of the bonds causes the release and conversion of their energy into the internal energy of each atom, leading the atomic temperature to rise [6, 28]. Another process is the process of applying heat by a laser. Since the thermal energy of the laser is applied to the atoms in the form of rotational kinetic energy, the local temperature of the atoms increases. According to the applied laser model, increasing the diameter and pulse intensity increases its kinetic energy and temperature. On the other hand, the lower advance speed prolongs the process of applying energy and transferring it to the subsurface layers. The temperature created in the system by the amorphous structure created in the contact area of the tool, which does not have good conductivity, is dissipated later and causes thermal softening [28].

6. Optimization

The laser-assisted nano-machining process is optimized for machining forces and hydrostatic stress. The reason for choosing these criteria is to minimize tool wear and structural changes to the workpiece. For this purpose, to achieve the least damage, the tool and the least structural changes of the workpiece are needed, so that the machining forces and hydrostatic stress have their lowest value, respectively. In this optimization, the temperature check is omitted because the maximum machining temperature seen in the SiC workpiece is lower than the structure destruction tempera-

ture, therefore, the temperature damage check to the workpiece structure is not meaningful. The method of performing the optimization process is based on the hill climbing method and the software used is Design Expert software. After applying all the conditions, the optimization results are shown in Fig. 26.

In the present optimization, the objective functions include minimizing the cutting force, minimizing the thrust force, and minimizing the hydrostatic stress of the workpiece. The design variables include the diameter, pulse intensity, and laser advance speed.

According to Fig. 26, it can be seen that the most optimal possible state in the simulations carried out in this research occurs when the value of the diameter, pulse intensity, and laser advance speed is 80nm, 109W/cm2, and 50m/s, respectively.

7. Comparison of Laser-assisted Nanomachining Process with the Conventional Nano-machining Process

After finding the optimal mode from the response surface method, the results of this mode are compared with the results of the conventional nano-machining process in the sixth section. The investigated results include machining force, machining surface temperature, and radial distribution function.

7.1. Comparison of Machining Force and Machining Surface Temperature

According to the diagram in Fig. 27, the diagram of thrust and cutting forces during machining according to the position of the tool, it can be seen that, in general, as the tool advances on the workpiece, the amount of machining force increases in both directions.

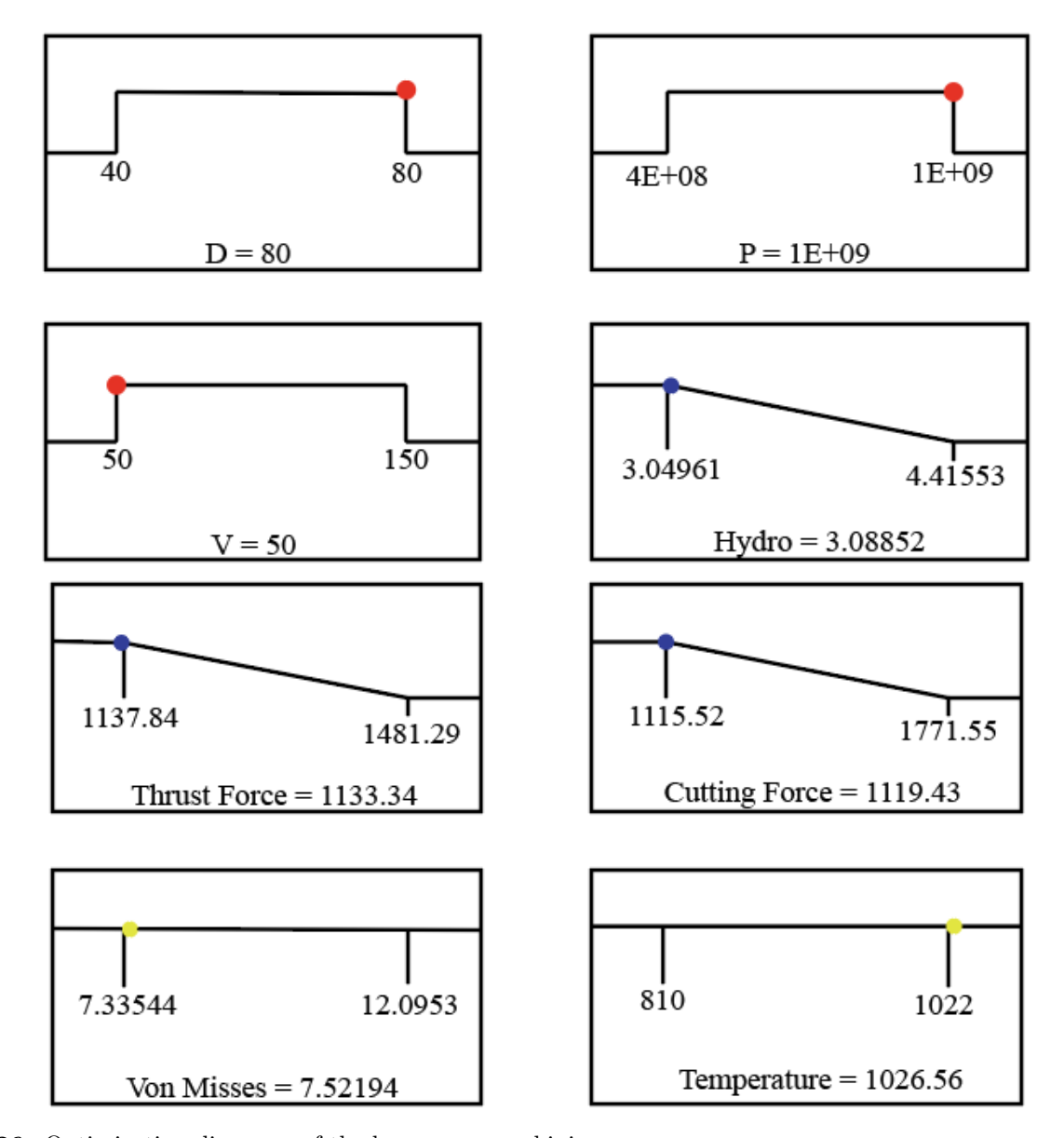


Fig. 26. Optimization diagrams of the laser nano-machining process.

The reason for this increase is the accumulation of atomic layers with an amorphous structure, these layers are created due to the chipping and destruction of the crystal structure, and their accumulation behind the tool increases machining forces.

On the other hand, by comparing the results, it is possible to see the effect of using a laser in the SiC nano-machining process. The machining forces are reduced by applying a laser on the machining surface and creating thermal softening phenomena, weakening the strength of covalent bonds between silicon and carbon atoms, and raising the interatomic energy level. Applying the laser causes an increase in the kinetic energy level and, as a result, an increase in the overall energy level among the atoms. Therefore, the increase in interatomic energy causes instability at the atomic level, which leads to their easy separation. According

to Fig. 28, it is clear that with laser application, the average temperature of the workpiece surface increases compared to conventional machining.

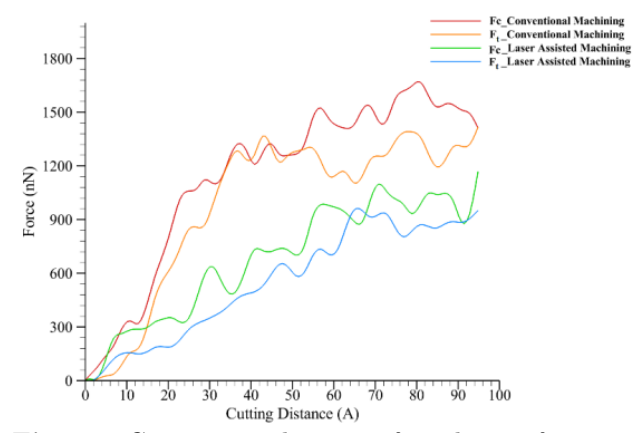


Fig. 27. Comparison diagram of machining forces.

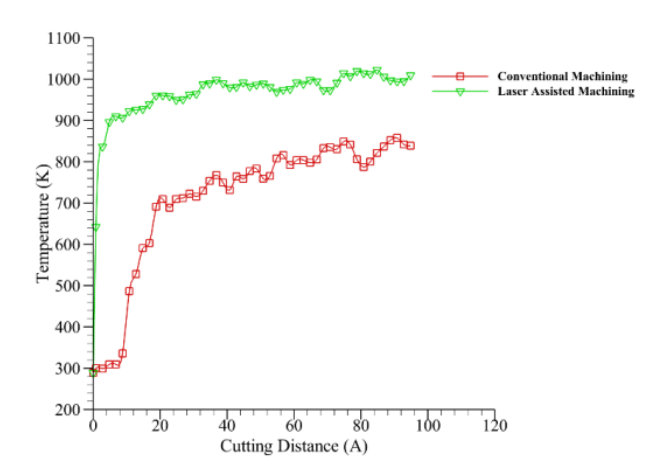


Fig. 28. Comparison chart of machining surface temperature.

7.2. Investigation of the Structural Changes of the Workpiece

To check the structural changes of the workpiece caused by laser-assisted nano-machining processes, the criterion of stress distribution function is used. This function is a measure of structural changes and the amount of atomic dispersion, which is calculated by calculating the density of the number of atoms around a specific atom. Since 99% of the deformation in the SiC workpiece is amorphous, this criterion can be a scale for the percentage of amorphization [14].

The radial distribution function of the SiC workpiece before and after both laser and conventional nano-machining processes are calculated to investigate the effect of each process on the structural changes. In Fig. 29, the radial distribution function of the workpiece before machining is plotted according to the interatomic distance. The selected radius is chosen to investigate the structure of 4.5 angstroms, and the reason for this choice is to cover all the interatomic bonds in the SiC network. In Fig. 29, four peaks at distances of 1.88, 3.07, 3.61, and 4.35 angstroms can be seen in the radial distribution diagram of the workpiece before nano-machining.

The diagram in Fig. 29 and its peaks correspond to the interatomic distances of siliconcarbon, silicon-silicon/carbon-carbon, silicon-carbon, and silicon-silicon atoms, respectively. This distribution indicates that the modeling is done and the selected potential function is correctly chosen.

The graph of the radial distribution function in each peak after both machining processes is shown in Figs. 30-33. Fig. 30 is related to the first peak and dispersion in the first type bond of silicon-carbon atoms. The fundamental changes in the structure are based on the changes in the peaks of this distribution. In the optimal state and before nano-machining, the value of this distribution is 32.78. After performing the laser-assisted nano-machining process and conventional nano-machining, the value of this distribution is 31.93 and 30.96, respectively. It is found that the laser-assisted nano-machining process produces fewer structural changes in this type of bond.

In Fig. 31, which is related to the second peak and dispersion in the first type of bond of silicon-silicon and carbon-carbon atoms, the effect of the conventional nano-machining process and laser-assisted nano-machining on the density of these bonds is investigated. In the optimal state and before nano-machining, the value of this distribution is 31.21. After performing the laser-assisted nano-machining process and conventional nano-machining, the value of this distribution is 33.35 and 35.96, respectively. Therefore, it is determined that the laser-assisted nano-machining process creates fewer structural changes in this type of bond.

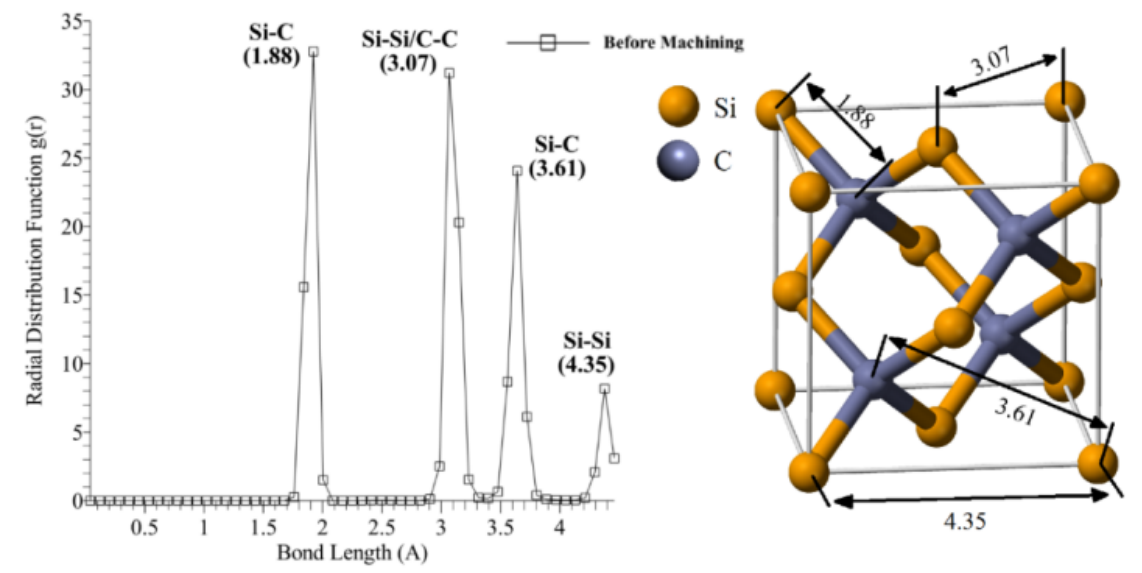


Fig. 29. Radial distribution function of the workpiece before machining.

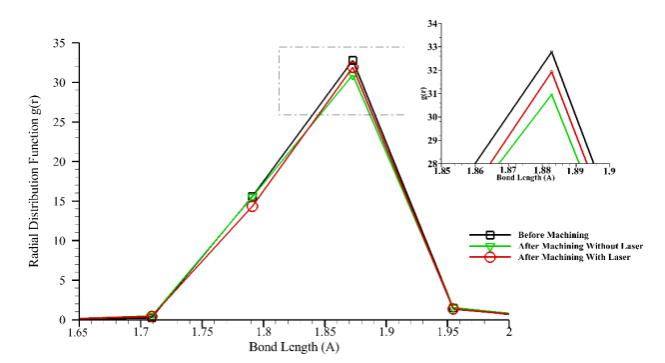


Fig. 30. Comparison diagram of the radial distribution function of the first peak.

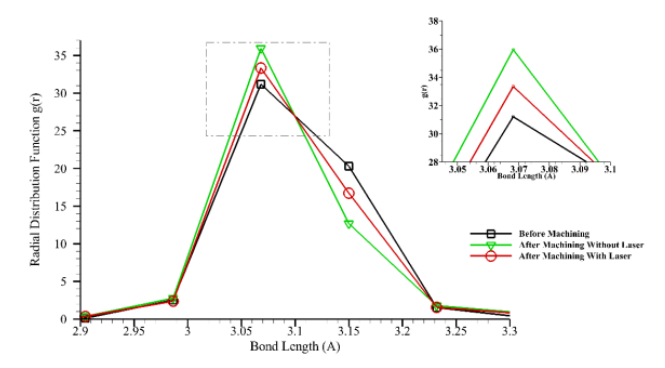


Fig. 31. Comparison diagram of the radial distribution function of the second peak.

Fig. 32 is related to the third peak and dispersion in the second type of silicon-carbon atoms bond. In the ideal state and before nano-machining, the value of this distribution is 24.07. After laser-assisted nano-machining and conventional nano-machining, the value of this distribution is 24.22 and 22.84, respectively. Therefore, it is determined that the laser-assisted nano-machining process does not create specific structural changes compared to conventional nano-machining in this type of bond.

Fig. 33 is related to the fourth peak and the dispersion in the type II bond of silicon-silicon type II atoms. In the ideal state and before nano-machining, the value of this distribution is 18.8. After laser-assisted nano-machining and conventional nano-machining, the value of this distribution is 8.29 and 8.28, respectively. It is found that laser-assisted nano-machining and conventional nano-machining produce similar structural changes in this type of bond. Finally, by examining and taking from all four graphs, it is concluded that the laser-assisted nano-machining process creates fewer structural changes in the material than conventional nano-machining.

8. Conclusions

This research was conducted to investigate the effect of laser components in the nano-machining process of single-crystal SiC and the simulation was done by the molecular dynamics method. After carrying out the simulations selected by the experiment design process, the behavior of this process was analyzed based on the components of diameter, pulse intensity, and laser advance speed, and the regression equations of the results were found. The optimized response obtained from this process was compared with the conventional machining process and the structural changes were investigated based on the criterion of the radial distribution function. The results are as follows: the cutting force of machining decreased from 1771.55 nanonewtons to 1115.52 nano-newtons by increasing the diameter, pulse intensity, and laser speed. The value of vertical machining force decreased from 1480.38 nanonewtons to 1137.84 nano-newtons with increasing diameter, pulse intensity, and laser advance speed. Also, the Von Mises stress value decreased from 12.09GPa to 7.34GPa with increasing diameter, pulse intensity, and laser advance speed. With the increase in diameter, the intensity of the laser pulse, and the decrease in laser advance speed, the hydrostatic stress decreased slightly, so the structure did not undergo many changes.

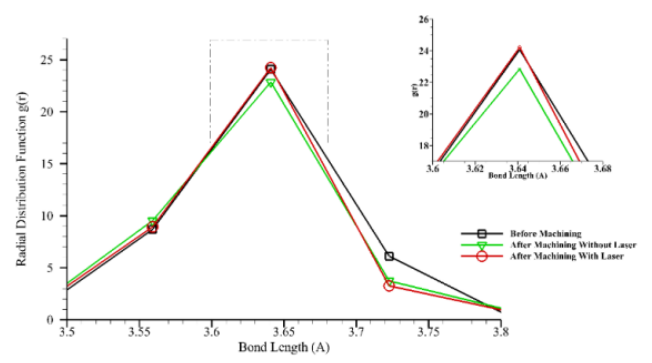


Fig. 32. Comparison diagram of the radial distribution function of the third peak.

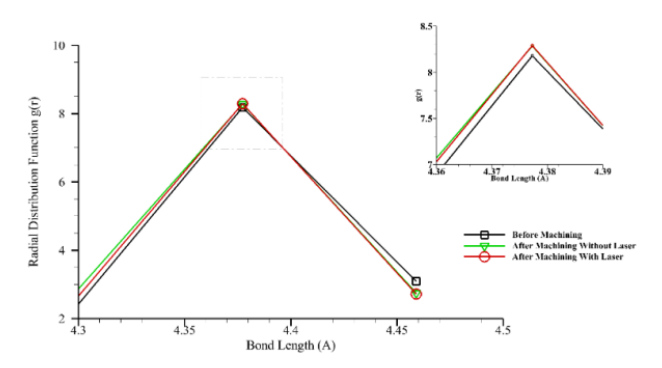


Fig. 33. Comparison diagram of the radial distribution function of the fourth peak.

An increase in the range of temperature between 810 and 1022 Kelvin was observed and this amount of temperature in the workpiece during this process did not cause much damage to it, but on the other hand, it caused the process of thermal softening in the SiC material. By comparing the laser-assisted nanomachining process and conventional nano-machining,

it was found that the machining forces in the laser- assisted nano-machining process are 35% less. The structural changes and damages observed in the workpiece in the laser-assisted nano-machining process were less than in the conventional nano-machining process.

References

- [1] A. O. Oluwajobi, "Nanomachining technology development," University of Huddersfield, 2012.
- [2] E. Brinksmeier et al., "Advances in modeling and simulation of grinding processes," CIRP annals, vol. 55, no. 2, pp. 667-696, 2006.
- [3] R. Rentsch, "Nanoscale cutting," Nano and Micromachining, pp. 1-26, 2009.
- [4] M. Chamani, "Three-dimensional multiscale modeling of nanoindentation," Journal of Molecular Graphics and Modelling, vol. 117, p. 108324, 2022.
- [5] S. Goel, X. Luo, R. L. Reuben, and W. B. Rashid, "Atomistic aspects of ductile responses of cubic silicon carbide during nanometric cutting," Nanoscale research letters, vol. 6, no. 1, pp. 1-9, 2011.
- [6] X. Luo, S. Goel, and R. L. Reuben, "A quantitative assessment of nanometric machinability of major polytypes of single crystal silicon carbide," Journal of the European Ceramic Society, vol. 32, no. 12, pp. 3423-3434, 2012.
- [7] S. Z. Chavoshi and X. Luo, "Molecular dynamics simulation study of deformation mechanisms in 3C-SiC during nanometric cutting at elevated temperatures," Materials Science and Engineering: A, vol. 654, pp. 400-417, 2016.
- [8] G. Xiao, S. To, and G. Zhang, "Molecular dynamics modelling of brittle-ductile cutting mode transition: case study on silicon carbide," International Journal of Machine Tools and Manufacture, vol. 88, pp. 214-222, 2015.
- [9] H. Dai and G. Chen, "A molecular dynamics investigation into the mechanisms of material removal and subsurface damage of nanoscale high speed laser-assisted machining," Molecular Simulation, vol. 43, no. 1, pp. 42-51, 2017.
- [10] Z. Wu, W. Liu, and L. Zhang, "Revealing the deformation mechanisms of 6H-silicon carbide under nano-cutting," Computational Materials Science, vol. 137, pp. 282-288, 2017.
- [11] B. Zhu et al., "A study on the surface quality and brittle-ductile transition during the elliptical vibration-assisted nanocutting process on

- monocrystalline silicon via molecular dynamic simulations," RSC advances, vol. 7, no. 7, pp. 4179-4189, 2017.
- [12] H. Dai, G. Chen, S. Li, Q. Fang, and B. Hu, "Influence of laser nanostructured diamond tools on the cutting behavior of silicon by molecular dynamics simulation," RSC advances, vol. 7, no. 25, pp. 15596-15612, 2017.
- [13] L. N. Abdulkadir and K. Abou-El-Hossein, "Observed edge radius behavior during MD nanomachining of silicon at a high uncut chip thickness," The International Journal of Advanced Manufacturing Technology, vol. 101, no. 5, pp. 1741-1757, 2019.
- [14] Y. Liu, B. Li, and L. Kong, "A molecular dynamics investigation into nanoscale scratching mechanism of polycrystalline silicon carbide," Computational Materials Science, vol. 148, pp. 76-86, 2018.
- [15] B. Meng, D. Yuan, J. Zheng, and S. Xu, "Molecular dynamics study on femtosecond laser aided machining of monocrystalline silicon carbide," Materials Science in Semiconductor Processing, vol. 101, pp. 1-9, 2019.
- [16] Z. Tian, X. Xu, F. Jiang, J. Lu, Q. Luo, and J. Lin, "Study on nanomechanical properties of 4H-SiC and 6H-SiC by molecular dynamics simulations," Ceramics International, vol. 45, no. 17, pp. 21998-22006, 2019.
- [17] L. Liu et al., "MD simulation of stress-assisted nanometric cutting mechanism of 3C silicon carbide," Industrial Lubrication and Tribology, 2019.
- [18] S. Goel, S. Z. Chavoshi, and A. Murphy, "Molecular dynamics simulation (MDS) to study nanoscale cutting processes," in Nanofinishing Science and Technology: CRC Press, 2016, pp. 519-568.
- [19] H. Dai, S. Li, and G. Chen, "Comparison of subsurface damages on mono-crystalline silicon between traditional nanoscale machining and laserassisted nanoscale machining via molecular dynamics simulation," Nuclear Instruments and Methods in Physics Research Section B: Beam Interactions with Materials and Atoms, vol. 414, pp. 61-67, 2018.
- [20] B. Liu, Y. Wang, H. Yang, and K. Jiang, "Effect of Laser Power on Nanocutting Mechanism of Silicon Carbide Ceramic: A Molecular Dynamics Simulation," Advanced Theory and Simulations, p. 2300613.
- [21] A. P. Thompson et al., "LAMMPS-a flexible simulation tool for particle-based materials modeling at the atomic, meso, and continuum scales,"

- Computer Physics Communications, vol. 271, p. 108171, 2022.
- [22] S. Goel, X. Luo, R. L. Reuben, and W. B. Rashid, "Atomistic aspects of ductile responses of cubic silicon carbide during nanometric cutting," Nanoscale research letters, vol. 6, pp. 1-9, 2011.
- [23] P. Erhart and K. Albe, "Analytical potential for atomistic simulations of silicon, carbon, and silicon carbide," Physical Review B, vol. 71, no. 3, p. 035211, 2005.
- [24] D. C. Montgomery, Design and analysis of experiments. John wiley & sons, 2017.
- [25] H. Dai, F. Zhang, and J. Chen, "A study of ultraprecision mechanical polishing of single-crystal silicon with laser nano-structured diamond abrasive by molecular dynamics simulation," International

- Journal of Mechanical Sciences, vol. 157, pp. 254-266, 2019.
- [26] W. Cheong and L. Zhang, "Molecular dynamics simulation of phase transformations in silicon monocrystals due to nano-indentation," Nanotechnology, vol. 11, no. 3, p. 173, 2000.
- [27] S. Goel, X. Luo, A. Agrawal, and R. L. Reuben, "Diamond machining of silicon: a review of advances in molecular dynamics simulation," International Journal of Machine Tools and Manufacture, vol. 88, pp. 131-164, 2015.
- [28] P.-Z. Zhu, C. Qiu, F.-Z. Fang, D.-D. Yuan, and X.-C. Shen, "Molecular dynamics simulations of nanometric cutting mechanisms of amorphous alloy," Applied surface science, vol. 317, pp. 432-442, 2014.